



HAL
open science

Pyrenoidal sequestration of cadmium impairs carbon dioxide fixation in a microalga

Florent Penen, M.-P. Isaure, Dirk Dobritzsch, Etienne Gontier, Hiram Castillo-Michel, Philippe Le Coustumer, Julien Malherbe, Dirk Schaumlöffel

► **To cite this version:**

Florent Penen, M.-P. Isaure, Dirk Dobritzsch, Etienne Gontier, Hiram Castillo-Michel, et al.. Pyrenoidal sequestration of cadmium impairs carbon dioxide fixation in a microalga. *Plant, Cell and Environment*, 2020, 43 (2), pp.479-495. 10.1111/pce.13674 . hal-02399338

HAL Id: hal-02399338

<https://hal.science/hal-02399338>

Submitted on 9 Dec 2020

HAL is a multi-disciplinary open access archive for the deposit and dissemination of scientific research documents, whether they are published or not. The documents may come from teaching and research institutions in France or abroad, or from public or private research centers.

L'archive ouverte pluridisciplinaire **HAL**, est destinée au dépôt et à la diffusion de documents scientifiques de niveau recherche, publiés ou non, émanant des établissements d'enseignement et de recherche français ou étrangers, des laboratoires publics ou privés.

28 ***Corresponding author:**

29 Dirk Schaumlöffel

30 CNRS / Université de Pau et des Pays de l'Adour / E2S UPPA, Institut des Sciences

31 Analytiques et de Physico-Chimie pour l'Environnement et les Matériaux, UMR 5254, 64000

32 Pau, France

33 Tel: (+33) 559 40 77 60

34 E-mail adress: dirk.schaumloeffel@univ-pau.fr

35 **ABSTRACT**

36 Mixotrophic micro-organisms are able to use organic as well as inorganic carbon sources and,
37 thus, play an essential role in the biogeochemical carbon cycle. In aquatic ecosystems, the
38 alteration of CO₂ fixation by toxic metals such as cadmium - classified as a priority pollutant -
39 could contribute to the unbalance of the carbon cycle. In consequence, the investigation of
40 cadmium impact on carbon assimilation in mixotrophic micro-organisms is of high interest.
41 We exposed the mixotrophic microalga *Chlamydomonas reinhardtii* to cadmium in a growth
42 medium containing both CO₂ and labeled ¹³C-[1,2] acetate as carbon sources. We showed that
43 the accumulation of cadmium in the pyrenoid, where it was predominantly bound to sulfur
44 ligands, impaired CO₂ fixation to the benefit of acetate assimilation. TEM/X-EDS and
45 μXRF/μXANES at Cd L_{III}-edge indicated the localization and the speciation of cadmium in the
46 cellular structure. In addition, NanoSIMS analysis of the ¹³C/¹²C ratio in pyrenoid and starch
47 granules revealed the origin of carbon sources. The fraction of carbon in starch originating
48 from CO₂ decreased from 73% to 39% during cadmium stress. For the first time, the
49 complementary use of high-resolution elemental and isotopic imaging techniques allowed
50 relating the impact of cadmium at the subcellular level with carbon assimilation in a
51 mixotrophic microalga.

52 **KEYWORDS**

53 Biogeochemical carbon cycle, CO₂ fixation, toxic metals, cadmium stress, subcellular imaging,
54 NanoSIMS, synchrotron μ XRF, μ XANES, TEM/X-EDS, isotopic labeling, isotope ratio

55

56 **INTRODUCTION**

57 The increase of carbon dioxide concentration in the atmosphere over the past decades has been
58 associated with global climate change. Therefore, investigation and understanding of the
59 biogeochemical carbon cycle is of primordial importance. The terrestrial and oceanic biosphere
60 plays a major role in the global carbon cycle by the production and conversion of organic matter
61 (Field, Behrenfeld, Randerson & Falkowski, 1998). Plants have developed a process for CO₂
62 fixation into organic carbon using the enzyme ribulose-1,5-bisphosphate
63 carboxylase/oxygenase (RuBisCO) which is regarded to be the most abundant protein in the
64 biosphere (Ellis, 1979). Microalgae are small eukaryotic organisms where RuBisCO is
65 concentrated in the specific organelle called the pyrenoid (Badger et al., 1998). Pyrenoid
66 containing algae have been identified as being responsible for 28 - 44% of the global carbon
67 fixation which underlines the key role of microalgae in the biogeochemical carbon cycle
68 (Mackinder et al., 2016).

69 Eukaryotic algae are classically considered as photoautotrophic using light and inorganic
70 compounds for energy and carbon fixation, or heterotrophic using only organic compounds.
71 Recently, mixotrophy has been integrated into aquatic biogeochemical cycle modeling (Caron,
72 2016; Ward & Follows, 2016). Mixotrophic organisms are able to combine photoautotrophic
73 growth conditions as well as heterotrophic nutrition. They are dominant among micro-algal
74 communities in oligotrophic and eutrophic environments (Burkholder, Glibert & Skelton,

75 2008; Hartmann et al., 2012). To date, the consideration of mixotrophy in biogeochemical
76 carbon cycle models is still at the beginning (Caron, 2016). Recently it has been shown that
77 mixotrophy globally lead to an increase of the size of organisms in the aquatic food chain and
78 thus enhances carbon sinking into the deep ocean by 35% (Ward & Follows, 2016).

79 Cadmium is a highly toxic metal and is considered as a priority pollutant in ecosystems
80 (Campbell, 2006). In high polluted natural waters micromolar cadmium concentrations were
81 found such as in the Tinto river in Spain (40 - 620 μM) (Aguilera & Amils, 2005) while for
82 other natural waters lower Cd concentration are described, e.g. 2.4 - 17.8 nM in polluted
83 Macedonian rivers (Ramani et al., 2014) and only 0.2 - 2 nM in a Swiss river (Xue & Sigg,
84 1998). Also, in polluted soils and soil solutions high cadmium concentrations were measured,
85 for example, 5.4 - 45.5 μM Cd in soil solutions of soils close to a chemical engineering plant
86 in Northern Taiwan (Lee, Lai & Chen, 2004) and 284 mg Cd per kg in paddy soils from
87 Thailand (Simmons, Pongsakul, Saiyasitpanich & Klinphoklap, 2005). Moreover, Cd has been
88 shown to be biomagnified in some aquatic food webs (Croteau, Luoma & Stewart, 2005;
89 Ikemoto et al., 2008; Rouleau, Gobeil & Tjlve, 2006; Signa, Mazzola, Tramati & Vizzini,
90 2017). At the microbial level, this accumulation occurs in communities between bacteria and
91 eukaryote organisms (Worden et al., 2015). In view of the importance of mixotrophy in the
92 aquatic carbon cycle, the impact of toxic metals such as Cd on carbon assimilation in
93 microalgae is of growing interest.

94 *Chlamydomonas reinhardtii* is a unicellular green alga which is found worldwide in soils and
95 fresh water as its natural habitat. This alga is used as a model for many cellular processes (Dent,
96 Han & Niyogi, 2001; Goto & Johnson, 1995; Harris, 1989; Merchant et al., 2006; Merchant,
97 Kropat, Liu, Shaw & Warakanont, 2012; Merchant et al., 2007; Rochaix, M. Goldschmidt-
98 Clermont & Merchant, 1998; Silflow & Lefebvre, 2001) including metallic stress (Hanikenne,

99 2003). Cadmium is known to inhibit its sexual reproduction (Goodenough et al., 1993), to limit
100 photosynthesis activity (Faller, Kienzler & Krieger-Liszkay, 2005; Nagel & Voigt, 1989, 1995;
101 Voigt & Nagel, 2002; Voigt, Nagel & Wrann, 1998) and to induce oxidative stress (Aksmann
102 et al., 2014; Vega, Garbayo, Domínguez & Vígara, 2006). In order to reduce free intracellular
103 Cd²⁺, the microalga synthesizes thiol peptides such as phytochelatins (Bräutigam,
104 Schaumlöffel, Preud'Homme, Thondorf & Wesenberg, 2011; Gekeler, Grill, Winnacker &
105 Zenk, 1988) and sequesters Cd bound to polyphosphate granules into vacuoles which were
106 compared to acidocalcisomes (Penen et al., 2017; Ruiz, Marchesini, Seufferheld, Govindjee &
107 Docampo, 2001).

108 *C. reinhardtii* can grow photoautotrophically in the presence of light and CO₂,
109 heterotrophically in the dark when acetate is available as an organic carbon source or
110 mixotrophically with acetate, CO₂ and light (Johnson & Alric, 2013). In the latter case, CO₂ is
111 photosynthetically fixed by RuBisCO (Johnson & Alric, 2012, 2013), while non-
112 photosynthetic acetate assimilation begins by its incorporation into acetyl coenzyme A
113 (acetylCoA) (Johnson & Alric, 2012, 2013). Then, acetylCoA is metabolized in the
114 tricarboxylic acid (TCA) cycle in mitochondria or in the glyoxylate cycle in cytosol (Johnson
115 & Alric, 2012, 2013; Singh, Shukla, Chary & Rao, 2014). Both acetate assimilation and
116 photosynthesis lead to starch formation (Ball, Dirick, Decq, Martiat & Matagne, 1990; Heifetz,
117 Förster, Osmond, Giles & Boynton, 2000; Johnson & Alric, 2012, 2013; Park et al., 2015). In
118 spite of an abundant literature about carbon assimilation under mixotrophic conditions in *C.*
119 *reinhardtii*, the impact of toxic metals on the carbon metabolism has not been investigated yet.

120 Ion beam and X-ray beam imaging techniques are powerful tools to study the isotopic and
121 elemental composition of single-cells (Ortega, Devès & Carmona, 2009; Penen et al., 2016;
122 Roschztardt et al., 2011; Sarret et al., 2013; Schaumlöffel et al., 2016). Nanoscale secondary

123 ion mass spectrometry (NanoSIMS) allows elemental and isotopic mapping with a resolution
124 of about 50 nm. In biology, it is used to localize and to determine at a subcellular level the
125 turnover of proteins and metabolites using stable isotopic tracers (^{13}C and ^{15}N) (Gao, Huang &
126 Tao, 2016; Lechene et al., 2006). Moreover, when NanoSIMS is combined with transmission
127 electron microscopy (TEM) in correlative imaging, isotopic tracers can be localized in the cell
128 structure (Clode, Stern & Marshall, 2007; Hoppe, Cohen & Meibom, 2013; Kopp et al., 2015;
129 Penen et al., 2016). NanoSIMS mapping has been also used to determine metal distributions in
130 plants and microalgae (Hong-Hermesdorf et al., 2014; Moore et al., 2010, 2011, 2012). As
131 complementary techniques, synchrotron micro X-ray fluorescence (μXRF) and micro X-ray
132 absorption spectroscopy (μXAS) can be combined and directly applied on frozen hydrated
133 samples to locate metals and decipher their structural environment, respectively, allowing the
134 determination of metal distribution and speciation in subcellular regions of microalgae (Adams
135 et al., 2016; Leonardo et al., 2014; Leonardo et al., 2016; Penen et al., 2017; Wang, Lv, Ma &
136 Zhang, 2016).

137 Here, we investigated the impact of cadmium on carbon assimilation in *C. reinhardtii* grown
138 under mixotrophic conditions. The objective was to relate subcellular cadmium localization
139 and speciation with acetate and CO_2 assimilation. Microalgae were thus exposed up to $70\ \mu\text{M}$
140 Cd and cultivated in the presence of labeled ^{13}C -[1,2] acetate to distinguish carbon originating
141 from acetate assimilation or from photosynthesis. A multimodal approach at subcellular level
142 allowed the localization of cadmium in the algal structure by TEM/X-EDS (X-ray energy
143 dispersive spectroscopy) and the determination of carbon origins by measuring the $^{13}\text{C}/^{12}\text{C}$ ratio
144 in the pyrenoid and starch using NanoSIMS. In addition, Cd was localized by μXRF , which
145 was combined to μXANES (micro X-ray absorption near edge structure spectroscopy) at the
146 Cd L_{III} -edge to identify Cd speciation. Our study showed that in *C. reinhardtii* cadmium
147 sequestration in the pyrenoid impaired CO_2 fixation to the benefit of acetate assimilation.

148 **MATERIALS AND METHODS**

149 **Biological material and growth conditions**

150 *Chlamydomonas reinhardtii* wild type strain (SAG 11/32b, Experimental Phycology and
151 Culture Collection of Algae at Goettingen University (EPSAG), Germany) was grown
152 heterotrophically in a tris-acetate-phosphate medium (Harris, 1989) where
153 ethylenediaminetetraacetic acid (EDTA) and $\text{FeSO}_4 \cdot 7\text{H}_2\text{O}$ were replaced by iron
154 ethylenediamine-N,N'-bis(2-hydroxyphenylacetate) (Fe-EDDHA) to increase the availability
155 of cadmium in solution. All chemicals and reagents were purchased from Sigma-Aldrich
156 (Saint-Quentin Fallavier, France) unless stated otherwise. The composition of this TAP_{EDDHA}
157 medium is described in Table S1. For carbon fixation experiments, the TAP_{EDDHA} (¹³C) medium
158 was prepared with ¹³C-labeled acetate (sodium ¹³C-[1,2] acetate, 99% ¹³C, Sigma Aldrich)
159 instead of acetic acid and pH was equilibrated to 7 with a HCl solution. Microalgae grew at 22
160 °C under constant illumination (by one Osram 827 and two Osram 840 fluorescent tubes) and
161 constant agitation (120 rpm). Fresh medium was inoculated with stock culture at the end of
162 exponential phase to reach an initial optical density at 730 nm (OD_{730nm}) of 0.040. Micro-algae
163 were exposed to 10, 20, 30, 40, 50 and 70 μM of CdCl₂ added 24 h after the inoculation while
164 control cultures were grown in parallel without Cd exposure (control). For controls and each
165 Cd concentration three independent algal cultures were grown (triplicates) and used for
166 replicated determination of the growth rate, chlorophyll and starch concentrations, and
167 cadmium uptake.

168 As the main aim of this study was the investigation of the cadmium stress response at cellular
169 level during the exponential growth phase, cells were exposed to Cd after 24h. Therefore
170 changes in the lag phase, the delay before the start of exponential growth, were not assayed
171 since this delay allowed the adaptation required for cells to begin the experience of new

172 environmental conditions, i.e. cadmium exposure in this study. The cell cycle of *C. reinhardtii*
173 is about 24 h which is confirmed with the start of the exponential phase at this time point. This
174 means that under these conditions the cells of the second (and third) cell cycle are exposed.
175 Cells were harvested after 72 h for different analyses, i.e. at the end of the third cell cycle when
176 these cells experienced similar exposure conditions. It is a good approximation although
177 cultivation was not synchronized. This procedure also applied in our previous studies
178 (Bräutigam, Schaumlöffel, Preud'Homme, Thondorf, & Wesenberg, 2011; Bräutigam,
179 Schaumlöffel, Krauss, & Wesenberg, 2009; Penen et al., 2017).

180 The concentrations of free metals in the medium were simulated (Table 1) with the freeware
181 Visual MINTEQ 3.0 (vminteq.lwr.kth.se/visual-minteq-ver-3-0/) (Gustafsson, 2013) using
182 Lindsay's database containing thermodynamic equilibrium constants compiled by Lindsay
183 (1979). Before use, glassware was washed with 5% HNO₃. All solutions were prepared with
184 ultrapure water (18 MΩ cm at 25 °C) obtained from a Milli-Q system (Millipore, Bedford,
185 MA).

186 **Growth rate determination**

187 Optical density at 730 nm (OD_{730nm}) was measured every 12 h in each control and Cd-exposed
188 algal cultures, grown in triplicate, using a spectrophotometer. Growth rates μ were calculated
189 as follows: $\mu = (\ln N_f - \ln N_i) / \Delta t$. N_f was the OD_{730nm} of the culture measured at the end of the
190 exponential phase. N_i was the OD_{730nm} of the culture at the beginning of the exponential phase
191 and Δt was the duration of the exponential phase (in days). Relative growth rate was expressed
192 as the ratio μ / μ_0 determined during the exponential phase of growth (μ : growth rate during
193 cadmium exposure, μ_0 : growth rate in control conditions). The Excel macro REGTOX
194 (http://www.normalesup.org/~vindimian/en_index.html) was used to calculate the half
195 maximal efficient concentrations (EC₅₀) applying the Hill model.

196 **Chlorophyll concentration measurement**

197 The chlorophyll concentration assay was adapted from Arnon *et al.* (Arnon, 1949). After 72 h
198 cultivation, 1 ml of each control and Cd-exposed algal cultures (grown in triplicate) was
199 centrifuged at $13000 \times g$ for 1 min. Each algal pellet was resuspended in 1 mL of 80% acetone
200 and vortexed for 2 min. Then, solubilized chlorophyll was separated from cell debris by a
201 centrifugation at $13000 \times g$ for 4 min. After that, the concentration (C) of chlorophyll a and b
202 in the culture medium was determined spectrophotometrically at 652 nm and calculated as
203 follows: $C = Ab_{652nm} \times 1000 / 34.5$ with C in $mg mL^{-1}$. Finally, in order to relate the chlorophyll
204 content to the biomass, the determined chlorophyll concentration was normalized to the optical
205 density at 730 nm whose value is proportional to the number of cells in the medium (unit: μg
206 $mL^{-1} OD_{730nm}^{-1}$).

207 **Starch concentration measurement**

208 After 72 h cultivation, microalgae were harvested from in triplicate grown control and Cd-
209 exposed ($70 \mu M$) algal cultures by centrifugation at $3000 \times g$ for 3 min and each pellet was
210 resuspended in 1.5 mL water. In order to estimate the dry biomass, a 0.5 mL aliquot from each
211 sample was dried at $60 \text{ }^{\circ}C$ for 24 h and the resulting pellet was weighted. The remaining 1 mL
212 samples were washed once with water and once with 80% ethanol, and centrifuged ($3000 \times g$
213 for 3 min). Then, each pellet was boiled in 2 mL water for 10 min. Finally, starch concentrations
214 were determined in these extracts, using the enzymatic starch assay kit HK (Sigma Aldrich)
215 described in Delrue *et al.* (1992).

216 **Cadmium uptake**

217 After 48 h cadmium exposure ($70 \mu M$), microalgae were harvested from in triplicate grown
218 cultures by centrifugation at $3000 \times g$ for 3 min. In order to obtain the intracellular Cd

219 concentration, each algal pellet was subjected to the following washing protocol according to
220 Macfie *et al.* (1994): a first time in water, then twice in a mix of Na₂-EDTA (1 mM) / CaCl₂
221 (3.77 mM) and finally in water with centrifugation between in (3000 × g for 3 min). The
222 remaining pellets were dried at 60°C for 24 h and weighted. This dry algal biomass was
223 digested in a mixture of 1 mL 70% (v/v) HNO₃ and 1 mL 30% (v/v) H₂O₂ at 80 °C for 3 h.
224 Samples were then diluted to reach a 2% HNO₃ concentration. The cadmium concentration
225 was determined by ICP-MS (Inductively Coupled Plasma Mass Spectrometry, 7500 model,
226 Agilent Technologies).

227

228 **Sample preparation for TEM/X-EDS and NanoSIMS**

229 Microalgae from a control and a Cd-exposed (70 μM) culture containing ¹³C-labeled acetate in
230 the medium were harvested after 72 h of inoculation by centrifugation at 3,000 × g for 3 min.
231 A protocol including high pressure freezing, and freeze substitution followed by resin inclusion
232 was used to preserve cell integrity. For high-pressure freezing, each microalgae pellet was
233 resuspended and incubated for 1 h in 150 mM mannitol. After a centrifugation at 3000 × g for
234 3 min, the harvested cells were included in agarose 2%. Then, the inclusion was plunged in
235 cryo-protectant 1-hexadecene and high-pressure freezing was performed immediately (EM
236 HPM 100, Leica Microsystems, Vienna, Austria). Samples were maintained in liquid nitrogen
237 until the freeze-substitution steps.

238 Freeze-substitution was adapted from O'Toole's protocol (O'Toole, 2010). Under liquid
239 nitrogen, algal samples were post-fixed in 1% osmium tetroxide, 0.1% uranyl acetate and
240 0.25% glutaraldehyde in anhydrous acetone and transferred into the Automatic Freeze
241 Substitution System AFS2 (Leica microsystems). Temperature was maintained at -90 °C for 3

242 d and then warmed to -30 °C for 8 h. Samples were removed from freeze-substitution system,
243 kept at 0 °C for 1 h and washed with water-free acetone.

244 Resin inclusion was carried out at room temperature. Samples were embedded in epoxy resin
245 (EPON 812, Delta Microscopies, Mauressac, France) using a graded resin and acetone series.
246 The following steps were applied for infiltration: 3:1 acetone:resin, 1:1 acetone:resin, 1:3
247 acetone:resin, and 2 baths with 100% resin. Finally, resin embedded samples were polymerized
248 for 48 h at 60 °C.

249 Samples were cut in 70 nm and 300 nm sections for TEM and NanoSIMS, respectively, using
250 a diamond knife (Diatome, Biel-Bienne, Switzerland) on an ultra-microtome [EM Ultracut-
251 UC7, Leica Microsystems) and placed on the respective sample holder. In order to carry out
252 correlative imaging by TEM and NanoSIMS, a first 70 nm section was placed on a copper grid
253 for TEM and then, an adjacent 300 nm section was placed on a silicon wafer (Wafer Solution,
254 Le Bourget du lac, France) for NanoSIMS as previously described (Penen et al., 2016). Cells
255 were localized and observed first by TEM and then, relocalized and analyzed by NanoSIMS.

256 **TEM/X-EDS analysis**

257 A transmission electron microscope FEI TECNAI 12 (Eindhoven, The Netherlands) using an
258 accelerating voltage 120 kV and equipped with an X-Energy Dispersive Spectroscopy (X-Flash
259 6T 60 BRUKER-SYNERGIE 4, Evry, France) was used. The parallel electron beam of the
260 nanoprobe was focused on 0.25-1.2 µm areas. Under these conditions X-EDS spectra of 1-2k
261 counts s⁻¹, a deadtime of 15-20% and analytical time of 120 - 240 s per spectrum were
262 generated.

263 **NanoSIMS analysis**

264 A nanoscale secondary ion mass spectrometer NanoSIMS 50L (CAMECA, Gennevilliers,
265 France) was used to perform SIMS analysis. This device was equipped with a primary Cs⁺ ion
266 source (lateral resolution down to 50 nm) for the mapping of electronegative elements, and
267 with a novel O⁻ RF plasma primary ion source enabling a high sensitivity for electropositive
268 elements combined to a high lateral resolution (40 nm lateral resolution) (Malherbe et al.,
269 2016). The seven parallel electron multiplier detectors equipped on the NanoSIMS 50L
270 instrument allowed detection of seven elements at the same time. In order to remove major
271 interferences on the chosen element masses, the mass resolution (M/ΔM) was tuned to be about
272 5000. Initially, ion maps (256×256 pixels, 64-144 μm²) of ¹²C⁻, ¹³C⁻, ¹²C¹⁴N⁻ (for N detection)
273 and ³²S⁻ were carried out using the primary Cs⁺ ion source. Mapping of ³¹P⁺ and ⁴⁰Ca⁺ was then
274 performed using the O⁻ RF plasma primary ion source.

275 **NanoSIMS data processing**

276 Image processing was performed using ImageJ software (v.1.48, Wayne Rasband, National
277 Institutes of Health (NIH), Bethesda, MD, USA). Processing of NanoSIMS images required
278 additionally the openMIMS plugin developed at the National Resource for Imaging Mass
279 Spectrometry (NRIMS, Cambridge, MA, USA). Ion maps were corrected for detector dead
280 time (44 ns) with the openMIMS plugin and the ¹³C/¹²C ratio maps were corrected for the mass
281 bias as a function of the ¹³C/¹²C ratio measured on microalgae not enriched in ¹³C. The ¹³C/¹²C
282 ratio was measured in regions of interest (ROI) defined on pyrenoid and starch granules of six
283 control cells and six Cd-exposed cells as detailed in Figure S1. The isotopic enrichment of ¹³C
284 was expressed as its relative abundance δ¹³C compared to the ¹³C natural isotopic abundance
285 and calculated using the following formula:

$$286 \quad \delta^{13}\text{C} = \frac{R_{\text{sample}}}{R_{\text{nat}}} - 1 \quad (1)$$

287 where R_{sample} is the measured $^{13}\text{C}/^{12}\text{C}$ ratio in the ROI of the cells and R_{nat} is the natural carbon
288 isotope ratio.

289 The origin of carbon in starch granules from either acetate or CO_2 as carbon source was
290 determined by data processing adapted from Terrado et al. (2017). First, the fractional
291 abundance F_{starch} of the carbon isotope ^{13}C in starch granules of the sum of both carbon isotopes
292 is given as (in percentage):

$$293 \quad F_{\text{starch}} = \frac{^{13}\text{C}}{^{13}\text{C} + ^{12}\text{C}} \times 100 \quad (2)$$

294 which can also be expressed as

$$295 \quad F_{\text{starch}} = \frac{R_{\text{starch}}}{1 + R_{\text{starch}}} \times 100 \quad (3)$$

296 where R_{starch} is the $^{13}\text{C}/^{12}\text{C}$ ratio measured in the ROI within starch granules. Then, the origin
297 of starch carbon was determined using the following formulas:

$$298 \quad F_{\text{starch}} = F_{\text{acetate}} \times f_{\text{acetate}} + F_{\text{CO}_2} \times f_{\text{CO}_2} \quad (4)$$

$$299 \quad \text{with: } f_{\text{acetate}} + f_{\text{CO}_2} = 1 \quad (5)$$

$$300 \quad f_{\text{acetate}} = \frac{F_{\text{starch}} - F_{\text{CO}_2}}{F_{\text{acetate}} - F_{\text{CO}_2}} \times 100 \quad \text{and} \quad f_{\text{CO}_2} = \frac{F_{\text{starch}} - F_{\text{acetate}}}{F_{\text{CO}_2} - F_{\text{acetate}}} \times 100 \quad (6)$$

301 The formula (6) results from (4) and (5) where F_{acetate} and F_{CO_2} are the fractional abundance of
302 ^{13}C in the carbon sources acetate (99%) and CO_2 (1.09%), respectively, and f_{acetate} and f_{CO_2}
303 represent the percentage of the origin of carbon within the ROI (starch granule) from the
304 respective source.

305 **Samples preparation for synchrotron-based techniques**

306 Microalgae from a control and a Cd-exposed (70 μM) culture were harvested after 72 h of
307 inoculation by centrifugation at $3000 \times g$ for 3 min. They were rapidly washed in ultrapure
308 water three times to remove metals and organic compounds weakly adsorbed on the cell wall.
309 Two sample preparations were used.

310 For μXRF and Cd L_{III} -edge μXANES , droplets of microalgae suspension were deposited on 4
311 μm -thick Ultralene film (SPEX sample prep Metuche, NJ). After decantation for 10 min,
312 microalgae were frozen into liquid nitrogen-chilled isopentane ($-160\text{ }^\circ\text{C}$).

313 For Cd L_{III} -edge XANES bulk analysis, the algae pellet was frozen in liquid nitrogen,
314 homogenized and pressed as a 5 mm frozen pellet. All the samples were kept frozen at $-80\text{ }^\circ\text{C}$
315 until measurements and transferred to the sample stage in their hydrated frozen state.

316

317 **μXRF imaging**

318 Measurements were performed on the ID21 beamline at the European Synchrotron Radiation
319 Facility (ESRF, Grenoble, France) equipped with a fixed exit Si(111) two-crystal
320 monochromator (Cotte et al., 2017). The X-ray photons were focused by a KB mirror system
321 providing a sub-micron resolution of $0.6\text{ }\mu\text{m}$ (H) \times $0.3\text{ }\mu\text{m}$ (V) FWHM on the sample. The X-
322 ray fluorescence signal was recorded with a large 100 mm^2 SDD detector (Bruker) while the
323 samples were scanned to obtain elemental maps. All the measurements were carried out under
324 cryogenic conditions at $-160\text{ }^\circ\text{C}$ using a liquid N_2 cryostat to limit beam radiation damage. The
325 fluorescence signal was normalized by the incident photon intensity (I_0) measured with a
326 photodiode. Phosphorus, sulfur, chloride, and cadmium maps were recorded using an incident
327 energy of 3570 eV, below the absorption edge of potassium, while potassium and calcium maps
328 were recorded at 4100 eV as described in Isaure *et al.* (2006). The fluorescence signal was

329 deconvoluted from fluorescence background and fluorescence elemental overlapping to obtain
330 elemental maps using the PYMCA software (Solé, Papillon, Cotte, Walter & Susini, 2007).

331 ***Cd L_{III}-edge μ XANES and XANES.*** μ XANES spectra were recorded with the same lateral
332 resolution as for μ XRF in fluorescence mode on points of interest visualized on the μ XRF
333 maps. For Cd model compounds and bulk samples, XANES spectra were recorded in
334 fluorescence mode with a defocused beam (100 μ m \times 100 μ m). Measurements were also done
335 under cryogenic conditions to limit radiation damage and speciation change. μ XANES and
336 XANES spectra were collected in the energy range 3520-3590 eV. Approximately 30 scans
337 were calibrated with a metallic Cd foil, averaged, and normalized according to standard
338 methods using ATHENA software (Ravel & Newville, 2005). Then, experimental normalized
339 spectra were compared to a library of standard spectra previously collected (Huguet et al.,
340 2012; Isaure et al., 2006, 2015; Penen et al., 2017). A fingerprint approach was used to simulate
341 the unknown spectra by linear combination fits (LCFs) of Cd model compounds as described
342 by Isaure *et al.* (2006). The quality of the fits was estimated by the normalized sum-squares
343 residuals $NSS = \frac{\sum(X_{anes_{experimental}} - X_{anes_{fit}})^2}{\sum(X_{anes_{experimental}})^2} \times 100$, in the 3520-3580 for
344 μ XANES spectra and 3520-3590 eV range for XANES spectra. Linear combination fits with
345 one, two and three components were tested and the combination with n+1 components was
346 retained if the NSS parameter decreased more than 20% in comparison to the fit with n
347 components (Figure S2). The uncertainty of the proportion of each compound was estimated
348 to 10% (Isaure et al., 2015).

349 **Statistics**

350 One-way ANOVA followed by a post-hoc Tuckey test Statistical analyses were performed on
351 growth rate, chlorophyll concentration, starch concentration and $^{13}C/^{12}C$ ratio measured on
352 NanoSIMS maps to identify significant differences among the different conditions. Results

353 were considered significant for a $p < 0.05$. Kruskal-Wallis one-way analysis of variance on
354 ranks ($p < 0.05$) was performed when the condition of homogeneity of variances was not
355 respected.

356 **RESULTS**

357 **Availability of cadmium and essential trace elements in TAP_{EDDHA} medium**

358 In a first approach, cadmium availability in TAP_{EDDHA} medium, i.e. free Cd²⁺ concentration,
359 was simulated using Visual Minteq software (Table 1). Concentrations of 10, 20, 30, 40, 50
360 and 70 µM of CdCl₂ added to the medium correspond to free ionic Cd concentrations of 1, 4,
361 7, 10, 13 and 20 µM. Cd availability was thus increased by 10 compared to the classic TAP
362 medium for the higher Cd concentration.

363 The free ion concentrations of several essential trace elements in the TAP_{EDDHA} medium were
364 markedly different from that in the original TAP medium (Table 1). Most important, the
365 concentration of free Zn²⁺ increased by 10000 and of free Cu²⁺ by 100 whereas Co²⁺ availability
366 decreased by 10000 compared to the classic TAP medium.

367 **Cadmium exposure leads to starch accumulation**

368 *C. reinhardtii* was exposed to a range of 10-70 µM CdCl₂ for 48 h in TAP_{EDDHA} medium and
369 relative growth rates were measured in order to determine Cd efficient concentrations (EC_x)
370 with the Hill model (Figure 1A). Up to 20 µM Cd, no significant effect on the algae growth
371 was observed (EC₅ = 22 µM Cd [15–31 µM Cd CI_{95%}]) but increasing Cd concentrations
372 induced a strong decrease of the relative growth rate (EC₅₀ = 74 µM Cd [67–86 µM Cd CI_{95%}]).
373 In order to investigate the impact of cadmium on *C. reinhardtii* in stress conditions, the Cd
374 exposure concentration of 70 µM (i.e. 20 µM free Cd²⁺) was applied in this study since it was
375 the nearest to EC₅₀ value. These concentrations can seem quite high compared to other studies

376 focused on Cd concentrations in the 10-100 nM range (Stoiber et al. 2012, Lavoie et al. 2012)
377 . However, contrary to these studies, the present experiments were carried out in mixotrophic
378 conditions, which likely modified the cell response. Our observations support that under
379 mixotrophic conditions *C. reinhardtii* was more resistant against Cd stress.

380 When exposed to 70 μM Cd, the intracellular cadmium concentration was $1530 \pm 132 \mu\text{g g}^{-1}$
381 (dry weight). The global impact of this cadmium stress on *C. reinhardtii* vitality was examined
382 by the determination of growth rate, chlorophyll concentration and starch concentration (Figure
383 1B, C and D). Compared to the control condition, Cd induced a decrease of the growth rate
384 (from 0.76 ± 0.05 to $0.39 \pm 0.06 \text{ d}^{-1}$) and the chlorophyll concentration (from 8.3 ± 0.4 to 6.4
385 $\pm 0.3 \mu\text{g mL}^{-1} \text{ OD}_{730\text{nm}}^{-1}$) while starch concentration was increased (from 47.6 ± 4.7 to $87.9 \pm$
386 13.2 mg g^{-1}). These results showed an important stress in *C. reinhardtii* when it exposed to 70
387 μM Cd leading to an impaired photosynthesis and an accumulation of starch. Carbon
388 metabolism in *C. reinhardtii* was thus strongly impacted by Cd toxicity.

389 **Cadmium sequestration in pyrenoid and vacuoles**

390 *C. reinhardtii* cells exposed to 70 μM Cd for 48 h were examined by TEM/X-EDS and
391 NanoSIMS (Figure 2). Figure 2 A and B show that cell structure was altered by Cd exposure,
392 particularly the chloroplast where the pyrenoid and its starch shell were destructured. The
393 starch plaques were also more abundant in the Cd-exposed cells corroborating the increase of
394 starch measured by enzymatic digestion.

395 Elemental composition of organelles observed on TEM micrographs (Figure 2C, F) was
396 determined on their corresponding NanoSIMS elemental maps (Figure 2E, H). Vacuoles were
397 rich in calcium, phosphorus and sulfur. Pyrenoids were characterized by a composition rich in
398 sulfur and nitrogen, which could be attributed to the high concentration in proteins (RuBisCO
399 in particular) inside this organelle. Moreover, pyrenoids were surrounded by a halo of

400 phosphorus which did not necessarily correspond to the starch shell. Finally, starch shells and
401 starch plates were rich in nitrogen.

402 Additional X-EDS analysis (Figure 2D, G) revealed that cadmium concentration was high in
403 the pyrenoid. This pyrenoidal sequestration of Cd could thus be responsible for Cd toxicity in
404 *C. reinhardtii*. Furthermore, Cd was localized beside Ca and P in electron dense bodies in
405 vacuoles suggesting a cadmium sequestration in calcium polyphosphate granules as confirmed
406 in our previous study by μ XANES analysis (Penen et al., 2017). It is important to note that the
407 elemental composition of vacuoles and pyrenoid determined by NanoSIMS was confirmed by
408 the X-EDS measurements.

409 **Cadmium localized in pyrenoid is preferentially bound to sulfur ligands**

410 Elemental μ XRF maps (Figure 3A) of *C. reinhardtii* cells exposed to 70 μ M Cd for 48 h
411 corroborated the elemental distribution obtained by TEM/X-EDS and NanoSIMS analysis
412 (Figure 3A). A sulfur spot was present in each cell which corresponded to the pyrenoid.
413 Although cadmium was detected at low level in the whole cells, it was highly concentrated in
414 one spot in each cell co-localized with sulfur, confirming its pyrenoidal sequestration. In
415 addition, phosphorus, calcium, and to a lesser extent cadmium were co-localized in spots of 1
416 μ m size representing Ca polyphosphate granules in vacuoles.

417 In combination with μ XRF, μ XANES gave information about Cd binding ligands in areas of
418 interest evidenced by μ XRF. In contrast, XANES collected in bulk samples allowed to
419 determine the average *in situ* cadmium binding in the microalgae. Cd L_{III}-edge XANES was
420 demonstrated powerful to distinguish sulfur from oxygen ligands due to absence of a peak at
421 3539 eV in sulfur binding atoms (Isaure et al., 2006). Moreover, as indicated by arrows in Cd
422 reference XANES spectra in figures 3B and 3C, the second oscillation was shifted to higher
423 energy values for Cd-acetate and Cd-malate where Cd is bound to carboxyl groups compared

424 to Cd bound to phosphate groups in Cd-phosphate and Cd-phytate (Penen et al., 2017). This
425 enabled a differentiation between the oxygen donor ligands in Cd-carboxyl and Cd-phosphate.
426 In contrast, Cd-phytochelatin 2 (Cd-PC₂), Cd-glutathione (Cd-GSH) and Cd-cysteine spectra
427 had similar pattern, thus hampering the exact determination of the nature of sulfur donor
428 ligands; however, they can be encompassed as thiol groups. Therefore, the distribution of Cd
429 ligands, as results of linear combination fits (LCFs) of Cd L_{III}-edge XANES and μ XANES
430 spectra, was described as ratios of Cd-S, Cd-O-P, and Cd-O-C compounds (Figure 3D).

431 In the S and Cd-enriched areas attributed to the pyrenoid, μ XANES analysis revealed that Cd
432 was mainly coordinated by thiol ligands ($67 \pm 10\%$ and $56 \pm 10\%$ for the two presented
433 pyrenoids), but also by carboxyl groups ($33 \pm 10\%$ and $44 \pm 10\%$). No phosphate ligand was
434 identified in these spots. A pyrenoid consists principally of proteins, mainly RuBisCO, thus
435 μ XANES results could indicate cadmium binding to protein thiol groups. Finally, Cd bound to
436 carboxyl groups could be attributed to Cd sequestered to the starch shell around the pyrenoid
437 since μ XANES here probed a three-dimensional volume.

438 XANES measurements of bulk samples showed that Cd- thiol ligands in algae accounted for
439 $31 \pm 10\%$ only while Cd- carboxyl groups amounted to $25 \pm 10\%$. The main part of Cd was
440 associated with phosphate ligands ($44 \pm 10\%$) suggesting that the calcium polyphosphate
441 granules sequestered an important part of the metal in *C. reinhardtii*. Indeed, these granules
442 were previously probed by μ XANES and revealed the sequestration of Cd by phosphate ligands
443 (Penen et al., 2017).

444 **Cadmium promotes carbon incorporation from acetate in starch**

445 In order to investigate the impact of Cd on carbon fixation and to distinguish inorganic and
446 organic carbon sources of *C. reinhardtii*, i.e. CO₂ and acetate, ¹³C labeled acetate was employed

447 for tracer experiments. *C. reinhardtii* control cells and cells exposed to 70 μM Cd for 48 h in
448 TAP_{EDDHA} medium containing ^{13}C labeled acetate were examined by NanoSIMS (Figure 4).
449 $^{13}\text{C}/^{12}\text{C}$ ratio maps highlight intracellular areas of carbon resulting from acetate assimilation
450 (high $^{13}\text{C}/^{12}\text{C}$ ratio) (Figure 4A and B).

451 Two different subcellular regions of interest (ROI) were selected in $^{13}\text{C}/^{12}\text{C}$ ratio maps (Figure
452 S1) to investigate carbon assimilation: the pyrenoid as organelle of CO_2 fixation and the starch
453 plates as a final storage form of carbon in *C. reinhardtii*. Based on data from ROI in 6 individual
454 control cells and 6 exposed cells (Figure S1), the ^{13}C isotopic enrichment $\delta^{13}\text{C}$ was calculated
455 as represented in Figure 4C. Hence, ^{13}C enrichment was found in the pyrenoid, but it did not
456 change significantly under Cd exposure. In contrast, starch plates showed a 5-fold higher ^{13}C
457 enrichment under Cd exposure than in unexposed cells. In particular, the study of carbon
458 isotopic distribution in starch as the final carbon storage form allowed the quantification of
459 carbon assimilation from CO_2 and acetate sources.

460 The determination of f_{acetate} and f_{CO_2} in starch granules revealed that, under control conditions,
461 73% of starch carbon came from CO_2 (^{12}C) and 27% from acetate (^{13}C) (RSD \pm 9%). In
462 contrast, Cd stress seemed to disturb CO_2 (^{12}C) assimilation which decreased to 39% while
463 acetate (^{13}C) assimilation contributed for 61% of starch carbon (Figure 4D) (RSD \pm 13%).
464 Moreover, when the isotopic distribution of starch carbon was combined with the starch
465 concentration previously analyzed (Figure 1D), it appeared that overall CO_2 carbon (^{12}C)
466 assimilation remained limited ($1.28 \pm 0.18 \text{ mmol } (^{12}\text{C}) \text{ g}^{-1}$ in control condition; 1.26 ± 0.43
467 $\text{mmol } (^{12}\text{C}) \text{ g}^{-1}$ under Cd exposure) (Figure 4E) relative to the highly increased starch
468 biosynthesis under Cd exposure. In contrast, acetate carbon (^{13}C) assimilation was about 4-fold
469 higher during Cd exposure ($0.48 \pm 0.15 \text{ mmol } (^{13}\text{C}) \text{ g}^{-1}$ under control conditions; 1.99 ± 0.47
470 $\text{mmol } (^{13}\text{C}) \text{ g}^{-1}$ under Cd exposure). These results suggest that Cd exposure interfered with CO_2

471 assimilation due to the Cd fixation in the pyrenoid possibly due to the Cd binding to protein
472 thiol groups.

473 **DISCUSSION**

474 **Effect of the culture medium on cell vitality**

475 *C. reinhardtii* was cultivated in a modified version of TAP medium where EDTA was replaced
476 with EDDHA (TAP_{EDDHA}) in order to increase Cd availability and, at the same time, Cd
477 toxicity. However, under control conditions, this modification induced already a decrease of
478 cell vitality. Indeed, in our previous work (Penen et al., 2017), *C. reinhardtii* grown in classic
479 TAP medium showed a higher growth rate ($1.15 \pm 0.03 \text{ d}^{-1}$) and a higher production of
480 chlorophyll ($10.78 \pm 0.38 \mu\text{g ml}^{-1} \text{ OD}_{730\text{nm}}^{-1}$) compared to the present study where microalgae
481 have been cultivated in TAP_{EDDHA} medium (Figure 1B, C). These effects of TAP_{EDDHA} medium
482 on cell vitality in control conditions could be explained by changes in the availability of some
483 trace elements compared to the classic TAP medium (Table 1). Indeed, higher availability
484 mainly of zinc but also, to a lesser extent, of copper, and in addition deficiency of cobalt was
485 found in the control TAP_{EDDHA} medium.

486 **Cell response to cadmium stress**

487 Cell vitality results showed that a 70 μM Cd exposure for 48 h induced a decrease of the
488 chlorophyll concentration, which is a well-known sign of photosynthesis impairment (Nagel &
489 Voigt, 1989; Collard & Matagne, 1990; Nagel & Voigt, 1995; Prasad, Drej, Skawińska &
490 Strałka, 1998). The degradation of the chlorophyll pool was concomitant with a growth
491 decrease and an increase of carbon storage in the form of starch. Usually, this stress reaction
492 has been described in *C. reinhardtii* during nitrogen (Ball et al., 1990; Cakmak et al., 2012),
493 phosphorus (Ball et al., 1990) and sulfur (Ball et al., 1990; Cakmak et al., 2012) starvation.

494 Moreover, Juergens et al. (2015, 2016) showed that starch was accumulated to maintain a
495 carbon pool during N-starvation instead of delaying photoinhibition and oxidative stress due
496 to energetic overflows from photosynthesis. In case of metallic stress, starch storage was
497 reported in *Chlamydomonas acidophila* (Nishikawa, Yamakoshi, Uemura & Tominaga, 2003)
498 exposed to 20 μ M Cd where the size of starch plates observed microscopically increased 2.43-
499 fold. Metal stress could thus induce, in an indirect way, symptoms similar to those of nutrient
500 starvation. Working with *C. reinhardtii*, Bräutigam et al. (2011) showed that Cd stress induced
501 the synthesis of thiol polypeptides like phytochelatins, resulting in a decrease in the
502 intracellular concentration of its precursors like glutathione, γ -EC and cysteine leading
503 presumably to a sulfur starvation. Although, sulfur supply by the medium should be sufficient
504 (Bräutigam et al., 2011), an intracellular sulfur deficiency is conceivable. Furthermore, a
505 proteomic study (Gillet, Decottignies, Chardonnet & Maréchal, 2006) revealed that enzymes
506 involved in sulfur metabolism were modified under Cd stress in order to promote the synthesis
507 of phytochelatins.

508

509

510 **Cadmium is bound to RuBisCO in pyrenoid and to phosphate in acidocalcisome**

511 For the first time, a pyrenoidal sequestration of Cd and its binding to sulfur ligands were clearly
512 observed in *C. reinhardtii*. In addition, high sulfur and nitrogen content indicated a high protein
513 concentration in the pyrenoid. A model of the impact of Cd sequestration on carbon fixation in
514 *C. reinhardtii* is proposed in Figure 5. Pyrenoids are essentially composed of the protein
515 RuBisCO (Borkhsenius, Mason & Moroney, 1998). They are the place of the carbon fixation
516 from CO₂ via the Calvin cycle (Harris, 1989). Beside RuBisCO, the enzyme RuBisCO-activase
517 is involved in this process (McKay, Gibbs & Vaughn, 1991). Thus, it can be hypothesized that

518 Cd binding to protein thiol groups interferes with CO₂ fixation in *C. reinhardtii*, for example
519 due to conformational changes caused by cadmium-thiol bonds. Indeed, it has been reported
520 that modifications at cysteines 449 and 459 of the RuBisCO large subunit induce a
521 conformational change and a decrease of its carboxylase activity (Marín-Navarro & Moreno,
522 2006). Moreover, the RuBisCO large subunit protein is down-regulated under Cd exposure
523 (Gillet et al., 2006). For higher plants, it has been shown that Cd impairs the CO₂ assimilation
524 rate by RuBisCO activity decrease, e.g. in the crop *Lactuca sativa* (Dias et al., 2012) and in
525 *Nicotiana rustica* (Afef, Leila, Donia, Houda & Chiraz, 2011).

526 In addition, TEM/X-EDS, μ XRF and Cd L_{III}-edge XANES measurements have shown that Cd
527 was also coordinated by phosphate ligands and localized in 0.5-1 μ m sized vacuoles containing
528 phosphorus and calcium. In our previous work (Penen et al., 2017), cadmium was shown to be
529 localized in vacuoles which were compared to acidocalcisomes due to their specific elemental
530 composition in phosphorus and calcium (Goodenough, Heiss, Roth, Rusch & Lee, 2019; Hong-
531 Hermesdorf et al., 2014; Komine, Eggink, Park & Hooper, 2000; Komine, Park, Wolfe &
532 Hooper, 1996; Ruiz et al., 2001).

533

534 **CO₂ fixation is impaired by cadmium stress**

535 Cadmium has been shown to disturb the light-dependent part of the photosynthesis (Faller et
536 al., 2005) but no study has previously focused on the impact of Cd on carbon assimilation. *C.*
537 *reinhardtii* is able to grow photoautotrophically using CO₂, heterotrophically using acetate in
538 the dark and mixotrophically using both carbon sources in the light. In the present study,
539 mixotrophic growth conditions under constant illumination induced carbon storage as starch
540 (Figure 1D). Moreover, NanoSIMS analysis revealed that, carbon from acetate was
541 accumulated in the pyrenoid and in starch granules (Figure 4B). The pathways involved in

542 acetate assimilation as well as the impact of cadmium on these pathways are discussed in the
543 next paragraphs and are represented in Figure 5.

544 The accumulation of carbon from acetate in the pyrenoid can be explained by the assimilation
545 of acetate through the tricarboxylic acid cycle (TCA). Indeed, acetate assimilation starts with
546 its incorporation into acetyl coenzyme A (acetyl-CoA), either directly converted by acetyl-CoA
547 synthetase, or in two steps with the successive action of acetate kinase and phosphate
548 acetyltransferase. Acetyl-CoA is used as substrate in the TCA cycle in mitochondria. The TCA
549 cycle produces ATP as well as NADH and releases the carbon of acetyl-CoA as CO₂ (Johnson
550 & Alric, 2013). Then, the mitochondrial carbonic anhydrase CaH4/5 (Raven, 2001) converts
551 CO₂ in bicarbonate which is carried to the pyrenoid by the CO₂ concentrating mechanism
552 (CCM) (Meyer & Griffiths, 2013). This latter is a combination of active carbon transporters
553 (Burow, Chen, Mouton & Moroney, 1996; Im & Grossman, 2002; Miura et al., 2004; Pollock,
554 Prout, Godfrey, Lemaire & Moroney, 2004), carbonic anhydrases (Moroney et al., 2011)
555 specific to cellular compartments and the soluble proteins (LCIB/LCIC) (Yamano et al., 2010)
556 allowing CO₂ trapping inside the pyrenoid. In the present work, the isotopic ratio of carbon
557 (¹³C enrichment) inside the pyrenoid was similar under control and exposure conditions (Figure
558 4C) showing that cadmium did not seem to disturb TCA cycle and CCM.

559 Starch biosynthesis involves the successive actions of ADP-glucose pyrophosphorylase
560 (AGPP) and starch synthase (SS) on the final product of the gluconeogenesis pathway (glucose-
561 1-phosphate (G1P)). Carbon from acetate enters gluconeogenesis in two different ways, once
562 incorporated into AcetylCoA. On the one hand, as mentioned in the previous paragraph,
563 AcetylCoA feeds the TCA cycle releasing CO₂. In the chloroplast, the two carbon sources thus
564 share the CO₂ fixation step by RuBisCO into the Calvin cycle pathway. The final product of
565 the Calvin cycle (glyceraldehyde-3-phosphate (G3P)) can enter the gluconeogenesis (Johnson

566 & Alric, 2013). On the other hand, Acetyl-CoA feeds the glyoxylate cycle which is a TCA
567 cycle where CO₂ releasing steps are by-passed (Johnson & Alric, 2012, 2013) in the cytosol.
568 Indeed, using AcetylCoA and isocitrate as substrates, isocitrate lyase produces glyoxylate and
569 succinate. This latter is successively converted in mitochondria to fumarate, malate,
570 oxaloacetate then phosphoenolpyruvate (PEP) which is exported to cytosol and enters the
571 gluconeogenesis pathway.

572 *C. reinhardtii* is able to assimilate inorganic carbon via PEP carboxylation by the two PEP
573 carboxylases CrPpc1/CrPpc2, leading to the production of oxaloacetate (Mamedov, Moellering
574 & Chollet, 2005). However, the algal PEP carboxylase activity is mainly anaplerotic and not
575 photosynthetic (Giordano, Norici, Forssen, Eriksson & Raven, 2003). Although the impact of
576 cadmium on PEPC activity is not established in *C. reinhardtii*, it has been shown that Cd
577 inhibits PEPC activity in higher plants like *Miscanthus* species (Guo et al., 2016) and *Zea mays*
578 (Wang, Zhao, Liu, Zhou, & Jin, 2009).

579 Despite ¹³C-[1,2] labeling of acetate, our experiments do not allow us to distinguish the
580 pathways taken by acetate carbons to be finally incorporated in starch. However, unlabeled
581 carbon assimilation from CO₂ can only pass by the Calvin cycle. In consequence, after a 48 h
582 Cd exposure, the relative decrease in ¹²C from 73 to 39% of starch carbon (Figure 4D) shows
583 that carbon fixation through Calvin cycle pathway is limited by Cd stress but not completely
584 inhibited. Hence, the high increase of starch biosynthesis under Cd stress (Figure 1D) is
585 achieved in mixotrophic conditions by an about 4-fold higher carbon assimilation from acetate.
586 However, the overall amount of carbon assimilation from CO₂ into starch remains limited in
587 relation to the increase of starch production (Figure 4E). Moreover, the decrease in chlorophyll
588 concentration (figure 1C) coupled with a massive accumulation of Cd in the pyrenoid (Figures

589 2D, G and 3A) seems to disturb not only the light-dependent reactions (Faller et al., 2005) but
590 also the light-independent reactions of photosynthesis.

591 In unexposed *C. reinhardtii* grown under mixotrophic conditions, 78% of total carbon (Heifetz
592 et al., 2000) has been found to be from CO₂ assimilation which is similar to the 73% of starch
593 carbon originating from CO₂ found in this work. Although Cd exposure and nutrient starvation
594 have a similar impact on starch accumulation, the limitation of CO₂ fixation is specific to Cd
595 stress, since during nitrogen starvation, 65% of starch carbon (Juergens et al., 2016) as well as
596 80% of total carbon (Juergens et al., 2016) are taken from an inorganic carbon source. In
597 addition, enzymes involved in Calvin cycle have been shown to be down-regulated under Cd
598 stress (phosphoglycerate kinase, ribose-5phosphate isomerase) while enzymes involved in
599 acetate assimilation were up-regulated as for the isocitrate lyase (Gillet et al., 2006) involved
600 in the glyoxylate cycle or the phosphoglycerate mutase (Gillet et al., 2006) taking part in
601 gluconeogenesis.

602 Using NanoSIMS in combination with ¹³C-labeled acetate it was possible to detect, localize,
603 and quantify ¹³C-labeled starch as end product within the cells. Although these are important
604 results, the limitation of this approach is, that between the acetate substrate and the end product
605 no other metabolites of the carbon metabolism pathway during cadmium stress were measured.
606 A metabolomic or a fluxomic approach would be necessary to complete our results with regard
607 to the overall carbon fixation and metabolism pathway involved during cadmium stress in *C.*
608 *reinhardtii*.

609 In conclusion, the present work shows that cadmium clearly impairs carbon assimilation in *C.*
610 *reinhardtii* grown in mixotrophic conditions. Due to the pyrenoidal sequestration of Cd, CO₂
611 fixation is limited during Cd exposure whereas acetate assimilation is favored. Mixotrophy
612 could thus allow phytoplankton surviving toxic metal pollution events. Although mixotrophy

613 seems to render aquatic ecosystems more resistant, the alteration of CO₂ fixation by toxic
614 metals could contribute to the unbalance of the biogeochemical carbon cycle.

615 **ACKNOWLEDGEMENTS**

616 The work was supported by funding from the French ‘Ministère de l’Enseignement Supérieur
617 et de la Recherche’ via the projects ANR-11-EQPX-0027 MARSS and ANR-10-INBS-04
618 FranceBioImaging, and a PhD fellowship for F.P. Furthermore, this work was supported by
619 the bilateral (German-French) DAAD - Campus France program PROCOPE funded by the
620 German ‘Bundesministerium für Bildung und Forschung (BMBF)’, the French ‘Ministère des
621 Affaires étrangères et du développement International (MAEDI)’ and ‘Ministère de
622 l’Education nationale, de l’Enseignement supérieur et de la Recherche (MENESR)’. We also
623 thank ESRF (Grenoble, France) for the provision of beamtime on ID21 beamline. The
624 microscopy was done in the Bordeaux Imaging Center, a service unit of the CNRS-INSERM
625 and Bordeaux University, member of the national infrastructure France BioImaging. The
626 authors thank kindly Prof. U. Johannngmeier and Dr. I. Bertalan from the University Halle-
627 Wittenberg (Germany) for providing *C. reinhardtii* wild type strain (11/32b).

628 **CONFLICT OF INTEREST**

629 The authors declare no conflict of interests.

630

631

632

633 **REFERENCES**

- 634 Adams, M. S., Dillon, C. T., Vogt, S., Lai, B., Stauber, J., & Jolley, D. F. (2016). Copper
635 Uptake, Intracellular Localization, and Speciation in Marine Microalgae Measured by
636 Synchrotron Radiation X-ray Fluorescence and Absorption Microspectroscopy.
637 *Environmental Science & Technology*, 50(16), 8827–8839.
- 638 Afef, N.-H., Leila, S., Donia, B., Houada, G., & Chiraz, C.-H. (2011). Relationship between
639 physiological and biochemical effects of cadmium toxicity in *Nicotiana rustica*.
640 *American Journal of Plant Physiology*, 6(6), 294–303.
- 641 Aguilera, A., & Amils, R. (2005). Tolerance to cadmium in *Chlamydomonas* sp. (Chlorophyta)
642 strains isolated from an extreme acidic environment, the Tinto River (SW, Spain).
643 *Aquatic Toxicology*, 75(4), 316–329.
- 644 Aksmann, A., Pokora, W., Baścik-Remisiewicz, A., Dettlaff-Pokora, A., Wielgomas, B.,
645 Dziadziuszko, M., & Tukaj, Z. (2014). Time-dependent changes in antioxidative
646 enzyme expression and photosynthetic activity of *Chlamydomonas reinhardtii* cells
647 under acute exposure to cadmium and anthracene. *Ecotoxicology and Environmental*
648 *Safety*, 110, 31–40.
- 649 Arnon, D. I. (1949). Copper Enzymes in Isolated Chloroplasts. Polyphenoloxidase in *Beta*
650 *Vulgaris*. *Plant Physiology*, 24(1), 1–15.
- 651 Badger, M. R., Andrews, T. J., Whitney, S. M., Ludwig, M., Yellowlees, D. C., Leggat, W., &
652 Price, G. D. (1998). The diversity and coevolution of Rubisco, plastids, pyrenoids, and
653 chloroplast-based CO₂-concentrating mechanisms in algae. *Canadian Journal of*
654 *Botany*, 76(6), 1052–1071.
- 655 Ball, S. G., Dirick, L., Decq, A., Martiat, J.-C., & Matagne, R. (1990). Physiology of starch
656 storage in the monocellular alga *Chlamydomonas reinhardtii*. *Plant Science*, 66(1), 1–
657 9.

658 Borkhsenius, O. N., Mason, C. B., & Moroney, J. V. (1998). The Intracellular Localization
659 of Ribulose-1,5-Bisphosphate Carboxylase/Oxygenase in *Chlamydomonas reinhardtii*.
660 *Plant Physiology*, *116*(4), 1585–1591.

661 Bräutigam, A., Schaumlöffel, D., Krauss, G.-J., & Wesenberg, D. (2009). Analytical approach
662 for characterization of cadmium-induced thiol peptides—a case study using
663 *Chlamydomonas reinhardtii*. *Analytical and Bioanalytical Chemistry*, *395*(6), 1737–
664 1747.

665 Bräutigam, A., Schaumlöffel, D., Preud'Homme, H., Thondorf, I., & Wesenberg, D. (2011).
666 Physiological characterization of cadmium-exposed *Chlamydomonas reinhardtii*.
667 *Plant, Cell and Environment*, *34*(12), 2071–2082.

668 Burkholder, J. M., Glibert, P. M., & Skelton, H. M. (2008). Mixotrophy, a major mode of
669 nutrition for harmful algal species in eutrophic waters. *Harmful Algae*, *8*(1), 77–93.

670 Burow, M. D., Chen, Z.-Y., Mouton, T. M., & Moroney, J. V. (1996). Isolation of cDNA clones
671 of genes induced upon transfer of *Chlamydomonas reinhardtii* cells to low CO₂. *Plant*
672 *Molecular Biology*, *31*(2), 443–448.

673 Cakmak, T., Angun, P., Demiray, Y. E., Ozkan, A. D., Elibol, Z., & Tekinay, T. (2012).
674 Differential effects of nitrogen and sulfur deprivation on growth and biodiesel feedstock
675 production of *Chlamydomonas reinhardtii*. *Biotechnology and Bioengineering*, *109*(8),
676 1947–1957.

677 Campbell, P. G. C. (2006). Cadmium-A priority pollutant. *Environmental Chemistry*, *3*(6),
678 387–388.

679 Caron, D. A. (2016). Mixotrophy stirs up our understanding of marine food webs. *Proceedings*
680 *of the National Academy of Sciences*, *113*(11), 2806–2808.

681 Clode, P. L., Stern, R. A., & Marshall, A. T. (2007). Subcellular imaging of isotopically labeled
682 carbon compounds in a biological sample by ion microprobe (NanoSIMS). *Microscopy*
683 *Research and Technique*, 70(3), 220–229.

684 Collard, J. M., & Matagne, R. F. (1990). Isolation and genetic analysis of *Chlamydomonas*
685 *reinhardtii* strains resistant to cadmium. *Applied and Environmental Microbiology*,
686 56(7), 2051–2055.

687 Cotte, M., Pouyet, E., Salomé, M., Rivard, C., Nolf, W. D., Castillo-Michel, H., Fabris, T.,
688 Monico, L., Janssens, K., Wang, T., Sciau, P., Verger, L., Cormier, L., Dargaud, O.,
689 Brun, E., Bugnazet, D., Fayard, B., Hesse, B., Real, A.E.P., Veronesi, G., Langlois, J.,
690 Balcar, N., Vandenberghe, Y., Solé, V.A., Kieffer, J., Barrett, R., Cohen, C., Cornu, C.,
691 Baker, R., Gagliardini, E., Papillon, E. & Susini, J. (2017). The ID21 X-ray and infrared
692 microscopy beamline at the ESRF: status and recent applications to artistic materials.
693 *Journal of Analytical Atomic Spectrometry*, 32(3), 477–493.

694 Croteau, M.-N., Luoma, S. N., & Stewart, A. R. (2005). Trophic transfer of metals along
695 freshwater food webs: Evidence of cadmium biomagnification in nature. *Limnology*
696 *and Oceanography*, 50(5), 1511–1519.

697 Delrue, B., Fontaine, T., Routier, F., Decq, A., Wieruszeski, J. M., Van Den Koornhuyse, N.,
698 Maddelein, M.L., Fournet, B. & Ball, S. (1992). Waxy *Chlamydomonas reinhardtii*:
699 monocellular algal mutants defective in amylose biosynthesis and granule-bound starch
700 synthase activity accumulate a structurally modified amylopectin. *Journal of*
701 *Bacteriology*, 174(11), 3612–3620.

702 Dent, R. M., Han, M., & Niyogi, K. K. (2001). Functional genomics of plant photosynthesis in
703 the fast lane using *Chlamydomonas reinhardtii*. *Trends in Plant Science*, 6(8), 364–371.

704 Dias, M. C., Monteiro, C., Moutinho-Pereira, J., Correia, C., Gonçalves, B., & Santos, C.
705 (2012). Cadmium toxicity affects photosynthesis and plant growth at different levels.
706 *Acta Physiologiae Plantarum*, 35(4), 1281–1289.

707 Ellis, R. J. (1979). The most abundant protein in the world. *Trends in Biochemical Sciences*,
708 4(11), 241–244.

709 Faller, P., Kienzler, K., & Krieger-Liszkay, A. (2005). Mechanism of Cd²⁺ toxicity: Cd²⁺
710 inhibits photoactivation of Photosystem II by competitive binding to the essential Ca²⁺
711 site. *Biochimica et Biophysica Acta (BBA) - Bioenergetics*, 1706(1–2), 158–164.

712 Field, C. B., Behrenfeld, M. J., Randerson, J. T., & Falkowski, P. (1998). Primary Production
713 of the Biosphere: Integrating Terrestrial and Oceanic Components. *Science*, 281(5374),
714 237–240.

715 Gao, D., Huang, X., & Tao, Y. (2016). A critical review of NanoSIMS in analysis of microbial
716 metabolic activities at single-cell level. *Critical Reviews in Biotechnology*, 36(5), 884–
717 890.

718 Gekeler, W., Grill, E., Winnacker, E.-L., & Zenk, M. H. (1988). Algae sequester heavy metals
719 via synthesis of phytochelatin complexes. *Archives of Microbiology*, 150(2), 197–202.

720 Gillet, S., Decottignies, P., Chardonnet, S., & Maréchal, P. L. (2006). Cadmium response and
721 redoxin targets in *Chlamydomonas reinhardtii*: a proteomic approach. *Photosynthesis*
722 *Research*, 89(2–3), 201–211.

723 Giordano, M., Norici, A., Forssen, M., Eriksson, M., & Raven, J. A. (2003). An Anaplerotic
724 Role for Mitochondrial Carbonic Anhydrase in *Chlamydomonas reinhardtii*. *Plant*
725 *Physiology*, 132(4), 2126–2134.

726 Goodenough, U., Heiss, A. A., Roth, R., Rusch, J., & Lee, J.-H. (2019). Acidocalcisomes:
727 Ultrastructure, Biogenesis, and Distribution in Microbial Eukaryotes. *Protist*, 170(3),
728 287–313.

729 Goodenough, U. W., Shames, B., Small, L., Saito, T., Crain, R. C., Sanders, M. A., &
730 Salisbury, J. L. (1993). The role of calcium in the *Chlamydomonas reinhardtii* mating
731 reaction. *Journal of Cell Biology*, *121*(2), 365–374.

732 Goto, K., & Johnson, C. H. (1995). Is the cell division cycle gated by a circadian clock? The
733 case of *Chlamydomonas reinhardtii*. *The Journal of Cell Biology*, *129*(4), 1061–1069.

734 Guo, H., Hong, C., Chen, X., Xu, Y., Liu, Y., Jiang, D., & Zheng, B. (2016). Different Growth
735 and Physiological Responses to Cadmium of the Three *Miscanthus* Species. *PLOS*
736 *ONE*, *11*(4), e0153475.

737 Gustafsson, J., Petter. (2013). Visual MINTEQ | Visual MINTEQ – a free equilibrium
738 speciation model. Retrieved March 31, 2017, from <http://vminteq.lwr.kth.se/>.

739 Hanikenne, M. (2003). *Chlamydomonas reinhardtii* as a eukaryotic photosynthetic model for
740 studies of heavy metal homeostasis and tolerance. *New Phytologist*, *159*(2), 331–340.

741 Harris, E. H. (1989). *The Chlamydomonas Sourcebook: Introduction to Chlamydomonas and*
742 *Its Laboratory Use*. Academic Press, Inc. San Diego.

743 Hartmann, M., Grob, C., Tarran, G. A., Martin, A. P., Burkill, P. H., Scanlan, D. J., & Zubkov,
744 M. V. (2012). Mixotrophic basis of Atlantic oligotrophic ecosystems. *Proceedings of*
745 *the National Academy of Sciences*, *109*(15), 5756–5760.

746 Heifetz, P. B., Förster, B., Osmond, C. B., Giles, L. J., & Boynton, J. E. (2000). Effects of
747 Acetate on Facultative Autotrophy in *Chlamydomonas reinhardtii* Assessed by
748 Photosynthetic Measurements and Stable Isotope Analyses. *Plant Physiology*, *122*(4),
749 1439–1446.

750 Hong-Hermesdorf, A., Miethke, M., Gallaher, S. D., Kropat, J., Dodani, S. C., Chan, J.,
751 Barupala, D., Domaille, D.W., Shirasaki, D.I., Loo, J.A., Weber, P.K., Pett-Ridge, J.,
752 Stemmler, T.L., Chang, C.J. & Merchant, S. S. (2014). Subcellular metal imaging

753 identifies dynamic sites of Cu accumulation in *Chlamydomonas*. *Nature Chemical*
754 *Biology*, 10(12): 1034–1042.

755 Hoppe, P., Cohen, S., & Meibom, A. (2013). NanoSIMS: Technical Aspects and Applications
756 in Cosmochemistry and Biological Geochemistry. *Geostandards and Geoanalytical*
757 *Research*, 37(2), 111–154.

758 Huguet, S., Bert, V., Laboudigue, A., Barthès, V., Isaure, M.-P., Llorens, I., Schat, H. & Sarret,
759 G. (2012). Cd speciation and localization in the hyperaccumulator *Arabidopsis halleri*.
760 *Environmental and Experimental Botany*, 82, 54–65.

761 Ikemoto, T., Tu, N. P. C., Okuda, N., Iwata, A., Omori, K., Tanabe, S., Tuyen, B.C. &
762 Takeuchi, I. (2008). Biomagnification of Trace Elements in the Aquatic Food Web in
763 the Mekong Delta, South Vietnam Using Stable Carbon and Nitrogen Isotope Analysis.
764 *Archives of Environmental Contamination and Toxicology*, 54(3), 504–515.

765 Im, C. S., & Grossman, A. R. (2002). Identification and regulation of high light-induced genes
766 in *Chlamydomonas reinhardtii*. *The Plant Journal*, 30(3), 301–313.

767 Isaure, M.-P., Fayard, B., Sarret, G., Pairis, S., & Bourguignon, J. (2006). Localization and
768 chemical forms of cadmium in plant samples by combining analytical electron
769 microscopy and X-ray spectromicroscopy. *Spectrochimica Acta Part B: Atomic*
770 *Spectroscopy*, 61(12), 1242–1252.

771 Isaure, M.-P., Huguet, S., Meyer, C.-L., Castillo-Michel, H., Testemale, D., Vantelon, D.,
772 Saumitou-Laprade, P., Verbruggen, N. & Sarret, G. (2015). Evidence of various
773 mechanisms of Cd sequestration in the hyperaccumulator *Arabidopsis halleri*, the non-
774 accumulator *Arabidopsis lyrata*, and their progenies by combined synchrotron-based
775 techniques. *Journal of Experimental Botany*, 66(11), 3201–3214.

776 Johnson, X., & Alric, J. (2012). Interaction between Starch Breakdown, Acetate Assimilation,
777 and Photosynthetic Cyclic Electron Flow in *Chlamydomonas reinhardtii*. *Journal of*
778 *Biological Chemistry*, 287(31), 26445–26452.

779 Johnson, X., & Alric, J. (2013). Central Carbon Metabolism and Electron Transport in
780 *Chlamydomonas reinhardtii*: Metabolic Constraints for Carbon Partitioning between
781 Oil and Starch. *Eukaryotic Cell*, 12(6), 776–793.

782 Juergens, M. T., Deshpande, R. R., Lucker, B. F., Park, J.-J., Wang, H., Gargouri, M., Holguin,
783 F.O., Disbrow, B., Schaub, T., Skepper, J.N., Kramer, D.M., Gang, D.R., Hicks, L.M.
784 & Shachar-Hill, Y. (2015). The Regulation of Photosynthetic Structure and Function
785 during Nitrogen Deprivation in *Chlamydomonas reinhardtii*. *Plant Physiology*, 167(2),
786 558–573.

787 Juergens, M. T., Disbrow, B., & Shachar-Hill, Y. (2016). The Relationship of Triacylglycerol
788 and Starch Accumulation to Carbon and Energy Flows during Nutrient Deprivation in
789 *Chlamydomonas reinhardtii*. *Plant Physiology*, 171(4), 2445–2457.

790 Komine, Y., Eggink, L. L., Park, H., & Hooper, J. K. (2000). Vacuolar granules in
791 *Chlamydomonas reinhardtii*: polyphosphate and a 70-kDa polypeptide as major
792 components. *Planta*, 210(6), 897–905.

793 Komine, Y., Park, H., Wolfe, G. R., & Hooper, J. K. (1996). Secretory granules in the
794 cytoplasm of a wall-less mutant of *Chlamydomonas reinhardtii* contain processed light-
795 harvesting complex apoproteins and HSP70. *Journal of Photochemistry and*
796 *Photobiology B: Biology*, 36(3), 301–306.

797 Kopp, C., Domart-Coulon, I., Escrig, S., Humbel, B. M., Hignette, M., & Meibom, A. (2015).
798 Subcellular Investigation of Photosynthesis-Driven Carbon Assimilation in the
799 Symbiotic Reef Coral *Pocillopora damicornis*. *mBio*, 6(1), e02299-14.

800 Lavoie, M., Fortin, C., & Campbell, P. G. C. (2012). Influence of essential elements on
801 cadmium uptake and toxicity in a unicellular green alga: The protective effect of trace
802 zinc and cobalt concentrations. *Environmental Toxicology and Chemistry*, *31*(7), 1445–
803 1452.

804 Lechene, C., Hillion, F., McMahon, G., Benson, D., Kleinfeld, A. M., Kampf, J. P., Distel, D.,
805 Luyten, Y., Bonventre, J., Hentschel, D., Park, K.M., Ito, S., Schwartz, M., Benichou,
806 G. & Slodzian, G. (2006). High-resolution quantitative imaging of mammalian and
807 bacterial cells using stable isotope mass spectrometry. *Journal of Biology*, *5*, 20.

808 Lee, T.-M., Lai, H.-Y., & Chen, Z.-S. (2004). Effect of chemical amendments on the
809 concentration of cadmium and lead in long-term contaminated soils. *Chemosphere*,
810 *57*(10), 1459–1471.

811 Leonardo, T., Farhi, E., Boisson, A.-M., Vial, J., Cloetens, P., Bohic, S., & Rivasseau, C.
812 (2014). Determination of elemental distribution in green micro-algae using synchrotron
813 radiation nano X-ray fluorescence (SR-nXRF) and electron microscopy techniques –
814 subcellular localization and quantitative imaging of silver and cobalt uptake by
815 *Coccomyxa actinabiotis*. *Metallomics*, *6*(2), 316–329.

816 Leonardo, T., Farhi, E., Pouget, S., Motellier, S., Boisson, A.-M., Banerjee, D., Rébeillé, F.,
817 den Auwer, C. & Rivasseau, C. (2016). Silver Accumulation in the Green Microalga
818 *Coccomyxa actinabiotis*: Toxicity, in Situ Speciation, and Localization Investigated
819 Using Synchrotron XAS, XRD, and TEM. *Environmental Science & Technology*,
820 *50*(1), 359–367.

821 Lindsay, W. L. (1979). *Chemical equilibria in soils*. John Wiley & Sons, New York.

822 Macfie, S. M., Tarmohamed, Y., & Welbourn, P. M. (1994). Effects of cadmium, cobalt,
823 copper, and nickel on growth of the green alga *Chlamydomonas reinhardtii*: The

824 influences of the cell wall and pH. *Archives of Environmental Contamination and*
825 *Toxicology*, 27(4), 454–458.

826 Mackinder, L. C. M., Meyer, M. T., Mettler-Altmann, T., Chen, V. K., Mitchell, M. C.,
827 Caspari, O., Rosenzweig, E.S.F., Pallesen, L., Reeves, G., Itakura, A., Roth, R.,
828 Sommer, F., Geimer, S., Mühlhaus, T., Schroda, M., Goodenough, U., Stitt, M.,
829 Griffiths, H. & Jonikas, M. C. (2016). A repeat protein links Rubisco to form the
830 eukaryotic carbon-concentrating organelle. *Proceedings of the National Academy of*
831 *Sciences*, 113(21), 5958–5963.

832 Malherbe, J., Penen, F., Isaure, M.-P., Frank, J., Hause, G., Dobritsch, D., Gontier, E.,
833 Horr ard, F., Hillion, F. & Schauml offel, D. (2016). A New Radio Frequency Plasma
834 Oxygen Primary Ion Source on Nano Secondary Ion Mass Spectrometry for Improved
835 Lateral Resolution and Detection of Electropositive Elements at Single Cell Level.
836 *Analytical Chemistry*, 88(14), 7130–7136.

837 Mamedov, T. G., Moellering, E. R., & Chollet, R. (2005). Identification and expression
838 analysis of two inorganic C- and N-responsive genes encoding novel and distinct
839 molecular forms of eukaryotic phosphoenolpyruvate carboxylase in the green
840 microalga *Chlamydomonas reinhardtii*. *The Plant Journal*, 42(6), 832–843.

841 Mar n-Navarro, J., & Moreno, J. (2006). Cysteines 449 and 459 modulate the reduction–
842 oxidation conformational changes of ribulose 1·5-bisphosphate carboxylase/oxygenase
843 and the translocation of the enzyme to membranes during stress. *Plant, Cell &*
844 *Environment*, 29(5), 898–908.

845 McKay, R. M. ., Gibbs, S. P., & Vaughn, K. C. (1991). RuBisCo activase is present in the
846 pyrenoid of green algae. *Protoplasma*, (162), 38–45.

847 Merchant, S. S., Allen, M. D., Kropat, J., Moseley, J. L., Long, J. C., Tottey, S., & Terauchi,
848 A. M. (2006). Between a rock and a hard place: Trace element nutrition in

849 Chlamydomonas. *Biochimica et Biophysica Acta (BBA) - Molecular Cell Research*,
850 1763(7), 578–594.

851 Merchant, S. S., Kropat, J., Liu, B., Shaw, J., & Warakanont, J. (2012). TAG, You're it!
852 Chlamydomonas as a reference organism for understanding algal triacylglycerol
853 accumulation. *Current Opinion in Biotechnology*, 23(3), 352–363.

854 Merchant, S. S., Prochnik, S. E., Vallon, O., Harris, E. H., Karpowicz, S. J., Witman, G. B., ...
855 Grossman, A. R. (2007). The Chlamydomonas Genome Reveals the Evolution of Key
856 Animal and Plant Functions. *Science*, 318(5848), 245–250.

857 Meyer, M., & Griffiths, H. (2013). Origins and diversity of eukaryotic CO₂-concentrating
858 mechanisms: lessons for the future. *Journal of Experimental Botany*, 64(3), 769–786.

859 Miura, K., Yamano, T., Yoshioka, S., Kohinata, T., Inoue, Y., Taniguchi, F., Asamizu, E.,
860 Nakamura, Y., Tabata, S., Yamato, K.T., Ohyama, K. & Fukuzawa, H. (2004).
861 Expression Profiling-Based Identification of CO₂-Responsive Genes Regulated by
862 CCM1 Controlling a Carbon-Concentrating Mechanism in Chlamydomonas
863 reinhardtii. *Plant Physiology*, 135(3), 1595–1607.

864 Moore, K. L., Schröder, M., Lombi, E., Zhao, F.-J., McGrath, S. P., Hawkesford, M. J.,
865 Shewry, P.R. & Grovenor, C. R. M. (2010). NanoSIMS analysis of arsenic and
866 selenium in cereal grain. *New Phytologist*, 185(2), 434–445.

867 Moore, K. L., Schröder, M., Wu, Z., Martin, B. G. H., Hawes, C. R., McGrath, S. P.,
868 Hawkesford, M.J., Ma, J.F., Zhao, F.-J. & Grovenor, C. R. M. (2011). High-Resolution
869 Secondary Ion Mass Spectrometry Reveals the Contrasting Subcellular Distribution of
870 Arsenic and Silicon in Rice Roots. *Plant Physiology*, 156(2), 913–924.

871 Moore, K. L., Zhao, F.-J., Gritsch, C. S., Tosi, P., Hawkesford, M. J., McGrath, S. P., Tosi, P.,
872 Hawkesford, M.J., McGrath, S.P., Shewry, P.R. & Grovenor, C. R. M. (2012).

873 Localisation of iron in wheat grain using high resolution secondary ion mass
874 spectrometry. *Journal of Cereal Science*, 55(2), 183–187.

875 Moroney, J. V., Ma, Y., Frey, W. D., Fusilier, K. A., Pham, T. T., Simms, T. A., DiMario, R.J.,
876 Yang, J. & Mukherjee, B. (2011). The carbonic anhydrase isoforms of *Chlamydomonas*
877 *reinhardtii*: intracellular location, expression, and physiological roles. *Photosynthesis*
878 *Research*, 109(1–3), 133–149.

879 Nagel, K., & Voigt, J. (1989). In Vitro Evolution and Preliminary Characterization of a
880 Cadmium-Resistant Population of *Chlamydomonas reinhardtii*. *Applied and*
881 *Environmental Microbiology*, 55(2), 526–528.

882 Nagel, K., & Voigt, J. (1995). Impaired photosynthesis in a cadmium-tolerant *Chlamydomonas*
883 mutant strain. *Microbiological Research*, 150(1), 105–110.

884 Nishikawa, K., Yamakoshi, Y., Uemura, I., & Tominaga, N. (2003). Ultrastructural changes in
885 *Chlamydomonas acidophila* (Chlorophyta) induced by heavy metals and polyphosphate
886 metabolism. *FEMS Microbiology Ecology*, 44(2), 253–259.

887 Ortega, R., Devès, G., & Carmona, A. (2009). Bio-metals imaging and speciation in cells using
888 proton and synchrotron radiation X-ray microspectroscopy. *Journal of The Royal*
889 *Society Interface*, 6(Suppl 5), S649–S658.

890 O’Toole, E. T. (2010). *Chlamydomonas*. *Cryopreparation methods for the 3-D analysis of*
891 *cellular organelles*. *Methods Cellular Biology*, 96, 71–91.

892 Park, J.-J., Wang, H., Gargouri, M., Deshpande, R. R., Skepper, J. N., Holguin, F. O., Juergens,
893 M.T., Shachar-Hill, Y., Hicks, L.M. & Gang, D. R. (2015). The response of
894 *Chlamydomonas reinhardtii* to nitrogen deprivation: a systems biology analysis. *The*
895 *Plant Journal*, 81(4), 611–624.

896 Penen, F., Isaure, M. P., Dobritzsch, D., Bertalan, I., Castillo-Michel, H., Proux, O., Gontier,
897 E., Le Coustumer, P. & Schaumlöffel, D. (2017). Pools of cadmium in *Chlamydomonas*

898 reinhardtii revealed by chemical imaging and XAS spectroscopy. *Metallomics*,9, 910-
899 923.

900 Penen, F., Malherbe, J., Isaure, M.-P., Dobritsch, D., Bertalan, I., Gontier, E., Le Coustumer,
901 P. & Schaumlöffel, D. (2016). Chemical bioimaging for the subcellular localization of
902 trace elements by high contrast TEM, TEM/X-EDS, and NanoSIMS. *Journal of Trace*
903 *Elements in Medicine and Biology*, 37, 62–68.

904 Pollock, S. V., Prout, D. L., Godfrey, A. C., Lemaire, S. D., & Moroney, J. V. (2004). The
905 Chlamydomonas reinhardtii proteins Ccp1 and Ccp2 are required for long-term growth,
906 but are not necessary for efficient photosynthesis, in a low-CO₂ environment. *Plant*
907 *Molecular Biology*, 56(1), 125–132.

908 Prasad, M. N. V., Drej, K., Skawińska, A., & Strałka, K. (1998). Toxicity of Cadmium and
909 Copper in Chlamydomonas reinhardtii Wild-Type (WT 2137) and Cell Wall Deficient
910 Mutant Strain (CW 15). *Bulletin of Environmental Contamination and Toxicology*,
911 60(2), 306–311.

912 Ramani, S., Dragun, Z., Kapetanović, D., Kostov, V., Jordanova, M., Erk, M., & Hajrulai-
913 Musliu, Z. (2014). Surface Water Characterization of Three Rivers in the Lead/Zinc
914 Mining Region of Northeastern Macedonia. *Archives of Environmental Contamination*
915 *and Toxicology*, 66(4), 514–528.

916 Ravel, B., & Newville, M. (2005). *ATHENA* , *ARTEMIS* , *HEPHAESTUS* : data analysis for
917 X-ray absorption spectroscopy using *IFEFFIT*. *Journal of Synchrotron Radiation*,
918 12(4), 537–541.

919 Raven, J. A. (2001). A role for mitochondrial carbonic anhydrase in limiting CO₂ leakage from
920 low CO₂-grown cells of Chlamydomonas reinhardtii. *Plant, Cell & Environment*,
921 24(2), 261–265.

922 Rochaix, J.-D., M. Goldschmidt-Clermont & Merchant, S. (1998). *The Molecular Biology of*
923 *Chloroplasts and Mitochondria in Chlamydomonas*. Kluwer Academic Publishers,
924 Dordrecht, The Netherlands.

925 Roschzttardtz, H., Grillet, L., Isaure, M.-P., Conéjéro, G., Ortega, R., Curie, C., & Mari, S.
926 (2011). Plant Cell Nucleolus as a Hot Spot for Iron. *Journal of Biological Chemistry*,
927 286(32), 27863–27866.

928 Rouleau, C., Gobeil, C., & Tjlve, H. (2006). Cadmium accumulation in coastal demersal fish.
929 *Marine Ecology Progress Series*, 311, 131–143.

930 Ruiz, F. A., Marchesini, N., Seufferheld, M., Govindjee, & Docampo, R. (2001). The
931 Polyphosphate Bodies of *Chlamydomonas reinhardtii* Possess a Proton-pumping
932 Pyrophosphatase and Are Similar to Acidocalcisomes. *Journal of Biological*
933 *Chemistry*, 276(49), 46196–46203.

934 Sarret, G., Smits, E. A. H. P., Michel, H. C., Isaure, M. P., Zhao, F. J. & Tappero, R. (2013).
935 Chapter One - Use of Synchrotron-Based Techniques to Elucidate Metal Uptake and
936 Metabolism in Plants. In D. L. Sparks (Ed.), *Advances in Agronomy* (pp. 1–82).

937 Schaumlöffel, D., Hutchinson, R., Malherbe, J., Le Coustumer, P., Gontier, E. & Isaure, M.-P.
938 (2016), Novel Methods for Bioimaging Including LA-ICP-MS, NanoSIMS, TEM/X-
939 EDS, and SXRF, In: *Metallomics: Analytical Techniques and Speciation Methods*, ed.
940 Michalke, B., John Wiley and Sons, ISBN 978-3-527-33969-3, Wiley-VCH Verlag
941 GmbH, Weinheim, pp. 83-116

942 Signa, G., Mazzola, A., Tramati, C. D., & Vizzini, S. (2017). Diet and habitat use influence Hg
943 and Cd transfer to fish and consequent biomagnification in a highly contaminated area:
944 Augusta Bay (Mediterranean Sea). *Environmental Pollution*, 230, 394–404.

945 Silflow, C. D., & Lefebvre, P. A. (2001). Assembly and Motility of Eukaryotic Cilia and
946 Flagella. Lessons from *Chlamydomonas reinhardtii*. *Plant Physiology*, *127*(4), 1500–
947 1507.

948 Simmons, R. W., Pongsakul, P., Saiyasitpanich, D., & Klinphoklap, S. (2005). Elevated levels
949 of cadmium and zinc in paddy soils and elevated levels of cadmium in rice grain
950 downstream of a zinc mineralized area in Thailand: implications for public health.
951 *Environmental Geochemistry and Health*, *27*(5–6), 501–511.

952 Singh, H., Shukla, M. R., Chary, K. V. R., & Rao, B. J. (2014). Acetate and Bicarbonate
953 Assimilation and Metabolite Formation in *Chlamydomonas reinhardtii*: A ¹³C-NMR
954 Study. *PLOS ONE*, *9*(9), e106457.

955 Solé, V. A., Papillon, E., Cotte, M., Walter, P., & Susini, J. (2007). A multiplatform code for
956 the analysis of energy-dispersive X-ray fluorescence spectra. *Spectrochimica Acta Part*
957 *B: Atomic Spectroscopy*, *62*(1), 63–68.

958 Stoiber, T. L., Shafer, M. M., & Armstrong, D. E. (2012). Relationships between surface-bound
959 and internalized copper and cadmium and toxicity in *Chlamydomonas reinhardtii*.
960 *Environmental Toxicology and Chemistry*, *31*(2), 324–335.

961 Terrado, R., Pasulka, A. L., Lie, A. A.-Y., Orphan, V. J., Heidelberg, K. B., & Caron, D. A.
962 (2017). Autotrophic and heterotrophic acquisition of carbon and nitrogen by a
963 mixotrophic chrysophyte established through stable isotope analysis. *The ISME*
964 *Journal*, *11*(9), 2022–2034.

965 Vega, J. M., Garbayo, I., Domínguez, M. J., & Vígara, J. (2006). Effect of abiotic stress on
966 photosynthesis and respiration in *Chlamydomonas reinhardtii*: Induction of oxidative
967 stress. *Enzyme and Microbial Technology*, *40*(1), 163–167.

- 968 Voigt, J., & Nagel, K. (2002). The donor side of photosystem II is impaired in a Cd²⁺-tolerant
969 mutant strain of the unicellular green alga *Chlamydomonas reinhardtii*. *Journal of Plant*
970 *Physiology*, 159(9), 941–950.
- 971 Voigt, J., Nagel, K., & Wrann, D. (1998). A Cadmium-tolerant *Chlamydomonas* Mutant Strain
972 Impaired in Photosystem II Activity. *Journal of Plant Physiology*, 153(5–6), 566–573.
- 973 Wang, H., Zhao, S. C., Liu, R. L., Zhou, W., & Jin, J. Y. (2009). Changes of photosynthetic
974 activities of maize (*Zea mays* L.) seedlings in response to cadmium stress.
975 *Photosynthetica*, 47(2), 277–283.
- 976 Wang, S., Lv, J., Ma, J., & Zhang, S. (2016). Cellular internalization and intracellular
977 biotransformation of silver nanoparticles in *Chlamydomonas reinhardtii*.
978 *Nanotoxicology*, 10(8), 1129–1135.
- 979 Ward, B. A., & Follows, M. J. (2016). Marine mixotrophy increases trophic transfer efficiency,
980 mean organism size, and vertical carbon flux. *Proceedings of the National Academy of*
981 *Sciences*, 113(11), 2958–2963.
- 982 Worden, A. Z., Follows, M. J., Giovannoni, S. J., Wilken, S., Zimmerman, A. E., & Keeling,
983 P. J. (2015). Rethinking the marine carbon cycle: Factoring in the multifarious lifestyles
984 of microbes. *Science*, 347(6223), 1257594.
- 985 Xue, H., & Sigg, L. (1998). Cadmium speciation and complexation by natural organic ligands
986 in fresh water. *Analytica Chimica Acta*, 363(2–3), 249–259.
- 987 Yamano, T., Tsujikawa, T., Hatano, K., Ozawa, S.-I., Takahashi, Y., & Fukuzawa, H. (2010).
988 Light and low-CO₂-dependent LCIB-LCIC complex localization in the chloroplast
989 supports the carbon-concentrating mechanism in *Chlamydomonas reinhardtii*. *Plant &*
990 *Cell Physiology*, 51(9), 1453–1468.

991

992

993

994 **TABLES**995 **Table 1:** Comparison of ion availability in classic TAP medium and TAP_{EDDHA} medium.

Metal ions	Free ion concentrations (M)			
	TAP		TAP _{EDDHA}	
	Control	70 μ M Cd	Control	70 μ M Cd
Ca ²⁺	2.5 10 ⁻⁵	2.6 10 ⁻⁵	2.6 10 ⁻⁵	2.6 10 ⁻⁵
Mg ²⁺	3.1 10 ⁻⁴	3.1 10 ⁻⁴	3.1 10 ⁻⁴	3.1 10 ⁻⁴
Fe ²⁺	5.6 10 ⁻⁹	5.0 10 ⁻⁷	-	-
Fe ³⁺	-	-	1.1 10 ⁻²²	1.2 10 ⁻²²
Zn ²⁺	2.4 10 ⁻¹⁰	3.0 10 ⁻⁶	3.1 10 ⁻⁶	3.1 10 ⁻⁶
Cu ²⁺	6.5 10 ⁻¹⁴	6.1 10 ⁻¹⁰	6.9 10 ⁻¹²	7.5 10 ⁻¹²
Co ²⁺	1.5 10 ⁻¹¹	2.0 10 ⁻⁷	5.6 10 ⁻¹⁵	4.7 10 ⁻¹⁵
Mn ²⁺	10.7 10 ⁻¹⁰	8.0 10 ⁻¹⁰	8.3 10 ⁻¹⁰	8.4 10 ⁻¹⁰
MoO ₄ ²⁻	5.6 10 ⁻⁶	1.1 10 ⁻⁸	5.6 10 ⁻⁶	1.1 10 ⁻⁹
Cd ²⁺	-	2.1 10 ⁻⁶	-	2.0 10 ⁻⁵

996

997

998

999

1000 **FIGURE CAPTIONS**1001 **Figure 1:** Impact of cadmium exposure to *C. reinhardtii* grown in TAP_{EDDHA} medium. (A)1002 Relative growth rate was expressed as the ratio μ/μ_0 determined during the exponential phase

1003 of growth after addition of 0, 10, 20, 30, 40, 50 and 70 μM of CdCl_2 . ($n=3 \pm \text{sd}$). μ = growth
1004 rate during cadmium exposure, μ_0 = growth rate in control conditions. Black curve represents
1005 the dose-response effect calculated with the Hill model. Impact of a 70 μM Cd exposure on
1006 growth (B) and on chlorophyll concentration (C), and starch concentration (D) after a 48 h
1007 exposure. Significant differences with respect to the control condition at a significance level of
1008 0.05 ($p<0.05$) are indicated by an asterisk (*).

1009 **Figure 2:** Structure and elemental composition of *C. reinhardtii* cells exposed to cadmium. (A)
1010 Electron micrographs of two *C. reinhardtii* cells in control condition and (B) of two cells
1011 exposed to 70 μM Cd for 48 h, scale bar = 1 μm . Abbreviations: N, nucleus; P, pyrenoid; S,
1012 starch; Th, thylakoid; CW, cell wall. (C to H) Correlative TEM/X-EDS and NanoSIMS
1013 imaging of two cadmium exposed *C. reinhardtii* cells: (C and F) Electron micrographs of *C.*
1014 *reinhardtii* cells exposed to 70 μM Cd for 48 h, white arrows show the area analyzed by X-
1015 EDS analysis, scale bar = 1 μm . Abbreviations: N, nucleus; P, pyrenoid; S, starch; Th,
1016 thylakoid; V, vacuole; CV, contractile vacuole; CW, cellwall. (E and H) Corresponding
1017 NanoSIMS elemental maps obtained by Cs^+ ion source ($^{12}\text{C}^{14}\text{N}^-$ for N detection, $^{32}\text{S}^-$) and O-
1018 RF plasma ion source ($^{31}\text{P}^+$, $^{40}\text{Ca}^+$), $10 \times 10 \mu\text{m}^2$ (E) and $12 \times 12 \mu\text{m}^2$ (H) fields of 256×256
1019 pixels, scale bar = 2 μm . (D and G) X-EDS spectra of vacuoles and pyrenoid located on electron
1020 micrographs, copper signal is produced by the copper grid

1021 **Figure 3:** In situ cadmium localization and speciation in *C. reinhardtii* exposed to 70 μM Cd
1022 for 48 in $\text{TAP}_{\text{EDDHA}}$ medium. (A) False color $\mu\text{-XRF}$ elemental maps of Cd, S, P and Ca, arrows
1023 show points of interest where $\mu\text{-XANES}$ analyses were performed, scale bar = 2 μm . Step size
1024 = 0.4 μm , dwell-time = 300 ms/pixel at 3570 eV for S, P, Cd and at 4100 eV for Ca. (B) Two
1025 or three components fits (dotted line) of Cd L_{III} -edge $\mu\text{-XANES}$ spectra (solid line) of points
1026 of interest marked by arrows and of bulk sample; (C) Derivative of Cd L_{III} -edge μXANES ; (D)

1027 Distribution of Cd ligands after normalization of the percentages to 100%. The uncertainty is
1028 estimated to $\pm 10\%$.

1029 **Figure 4:** Carbon assimilation in *C. reinhardtii* grown in TAP_{EDDHA} medium (labeled ^{13}C -[1,2]
1030 acetate). (A and B) $^{13}\text{C}/^{12}\text{C}$ isotope ratio images obtained by NanoSIMS using Cs^+ source. The
1031 analyzed fields of 256×256 pixels were, from left to right, $12 \times 12 \mu\text{m}^2$, $8 \times 8 \mu\text{m}^2$, $10 \times 10 \mu\text{m}^2$
1032 for control conditions (A) and $12 \times 12 \mu\text{m}^2$, $10 \times 10 \mu\text{m}^2$, $10 \times 10 \mu\text{m}^2$ for cadmium exposure
1033 conditions ($70 \mu\text{M}$ Cd for 48 h) (B), scale bar = $2 \mu\text{m}$, ROI and annotations for pyrenoid and
1034 starch plates are shown in Figure S1. (C) Impact of $70 \mu\text{M}$ Cd exposure for 48 h on ^{13}C isotopic
1035 enrichment in the pyrenoid and in starch plates ($n=6 \pm \text{sd}$). Isotopic distribution of carbon in
1036 starch plates obtained from f_{acetate} and f_{CO_2} (D) and in starch carbon equivalent (E), ($n=6 \pm \text{sd}$).
1037 Significant differences with respect to the control condition according to Kruskal-Wallis one-
1038 way analysis of variance on ranks ($p < 0.05$) are indicated by an asterisk (*).

1039 **Figure 5:** Proposed model of cadmium impact on the assimilation of carbon in
1040 *Chlamydomonas reinhardtii* in mixotrophic conditions. The description of the general
1041 metabolic pathways for carbon assimilation from organic (acetate) and inorganic (CO_2) sources
1042 are adapted from Johnson & Alric (2013). Under exposure conditions, cadmium is highly
1043 sequestered in the pyrenoid by sulfur ligands, impairing the Calvin cycle. Thus, CO_2 and
1044 acetate assimilation involving the Calvin cycle is limited (thin grey arrows) whereas acetate
1045 assimilation through glyoxylate cycle is favored (thick blue arrows). In addition, the
1046 anaplerotic PEPC activity could hypothetically participate in inorganic carbon fixation. Starch
1047 is accumulated in the chloroplast to prevent cellular troubles due to Cd stress. Finally, Cd is
1048 also sequestered in vacuoles, coordinated by phosphate ligands. Abbreviations: *SDH*,
1049 Succinate dehydrogenase; *FUM*, Fumarase; *MDH*, Malate Dehydrogenase; *PCK*,

1050 Phosphoenolpyruvate Carboxykinase; *PEPC*, Phosphoenolpyruvate carboxylase; *CAH*,
1051 Carbonic anhydrase.

1052

1053 **SUPPORTING INFORMATION**

1054 Supporting information is available at the publisher's web-site. Supporting information is given
1055 to the composition of the TAP_{EDDHA} medium (**Table S1**), to the definition of regions of interest
1056 (ROI) in NanoSIMS ¹³C/¹²C images for data analysis (**Figure S1**), and to linear combination
1057 fits (LCFs) of XANES spectra (**Figure S2**).

1058

1059

1060

1061

1062

1063

1064

1065

1066

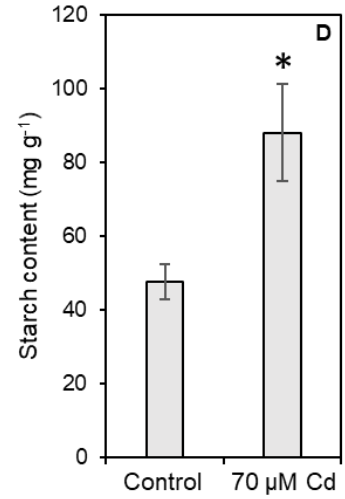
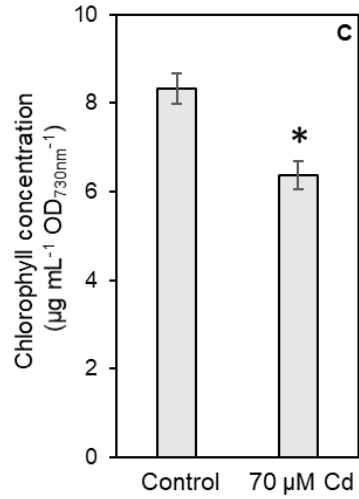
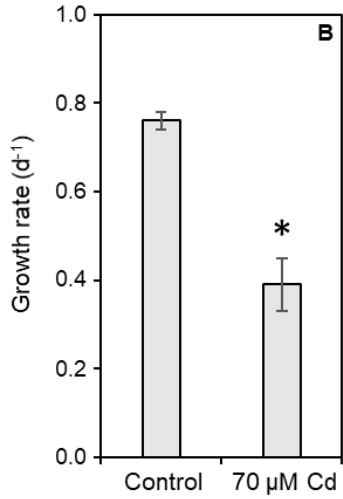
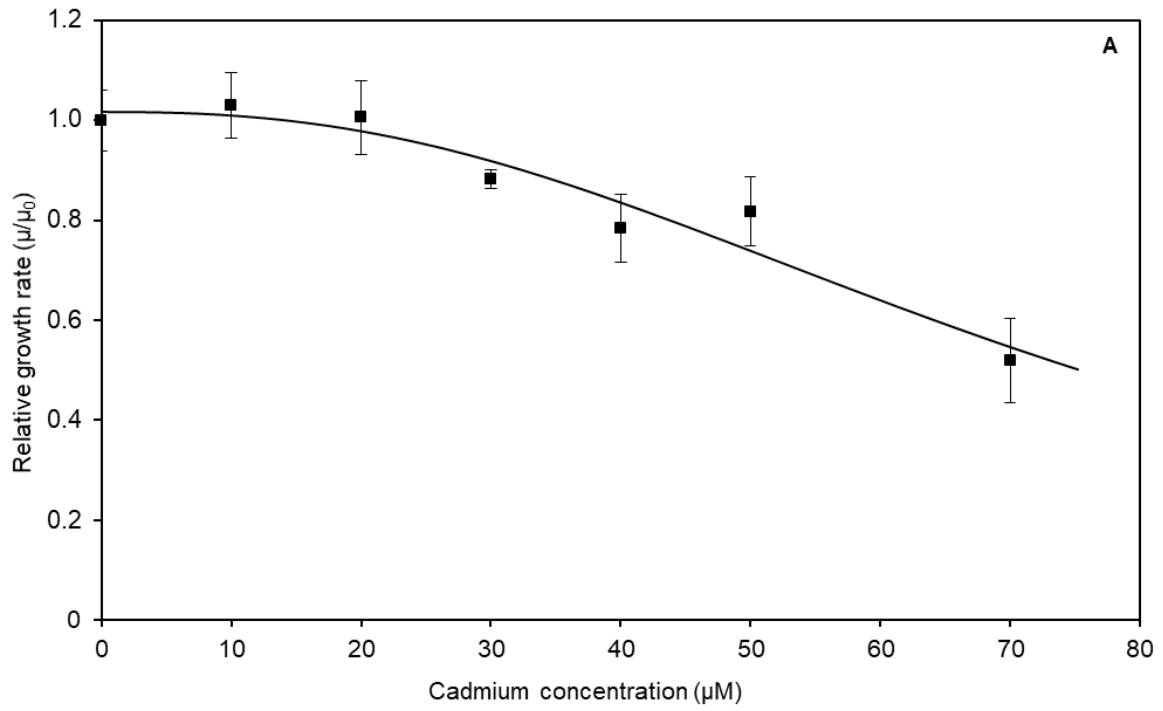
1067

1068

1069

1070

Figure 1



1071

1072

1073

1074

1075

1076

1077
 1078
 1079
 1080
 1081
 1082
 1083
 1084
 1085
 1086
 1087
 1088
 1089
 1090
 1091
 1092
 1093
 1094
 1095
 1096
 1097
 1098
 1099
 1100
 1101

Figure 2

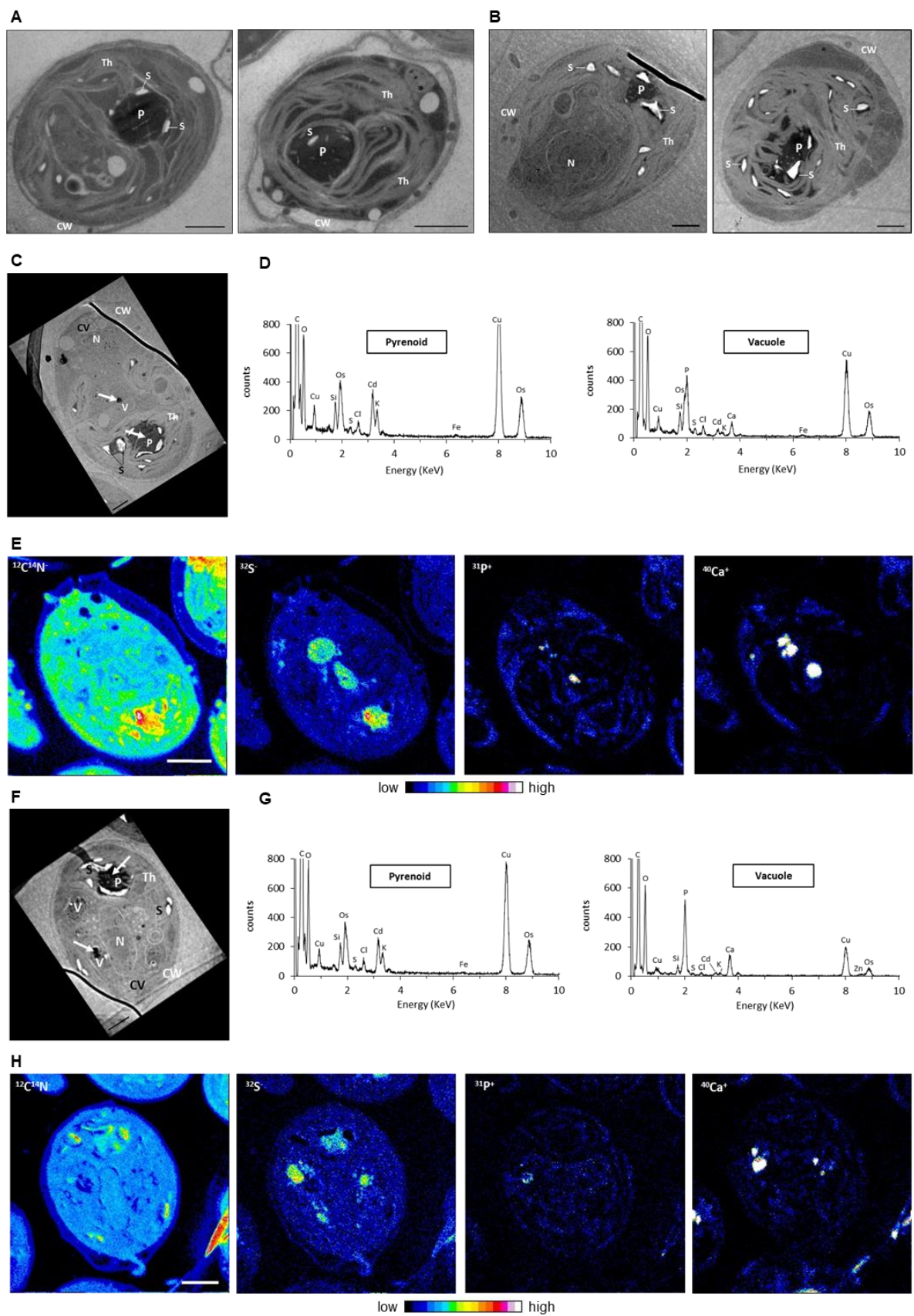
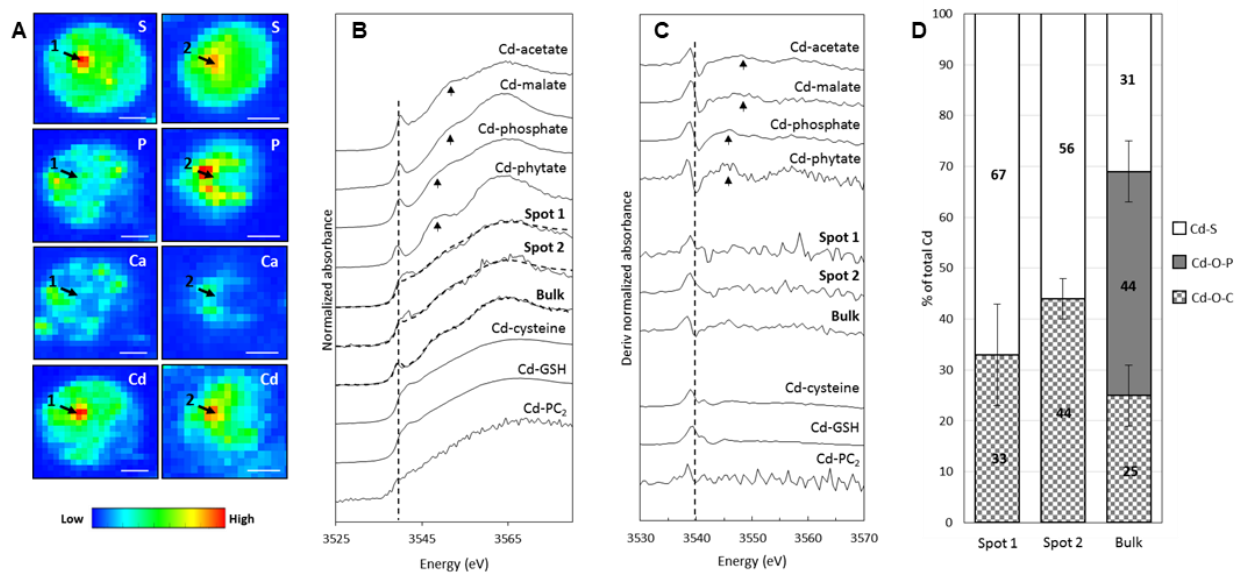


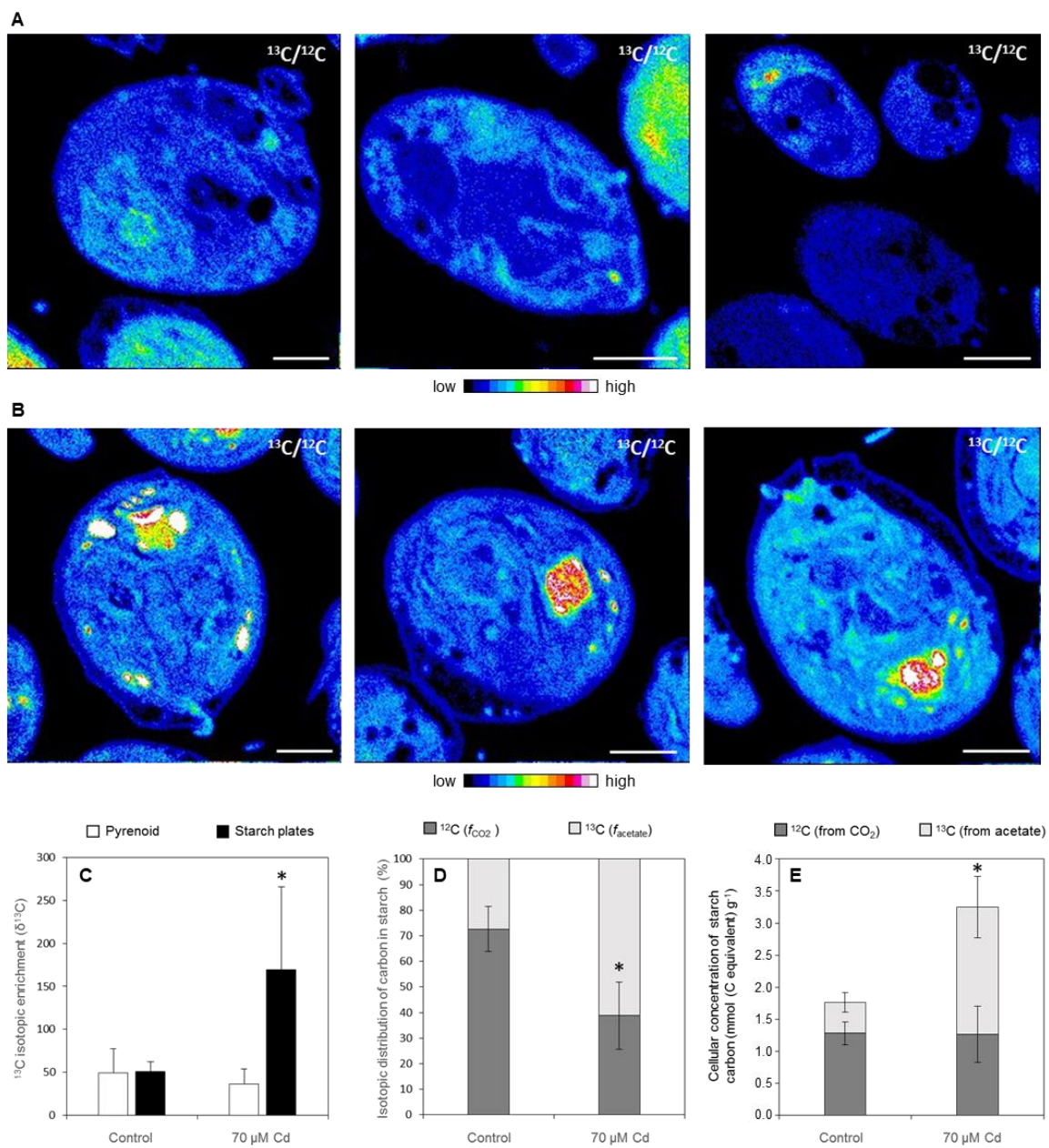
Figure 3



1102

1103

Figure 4



1104

1105

1106

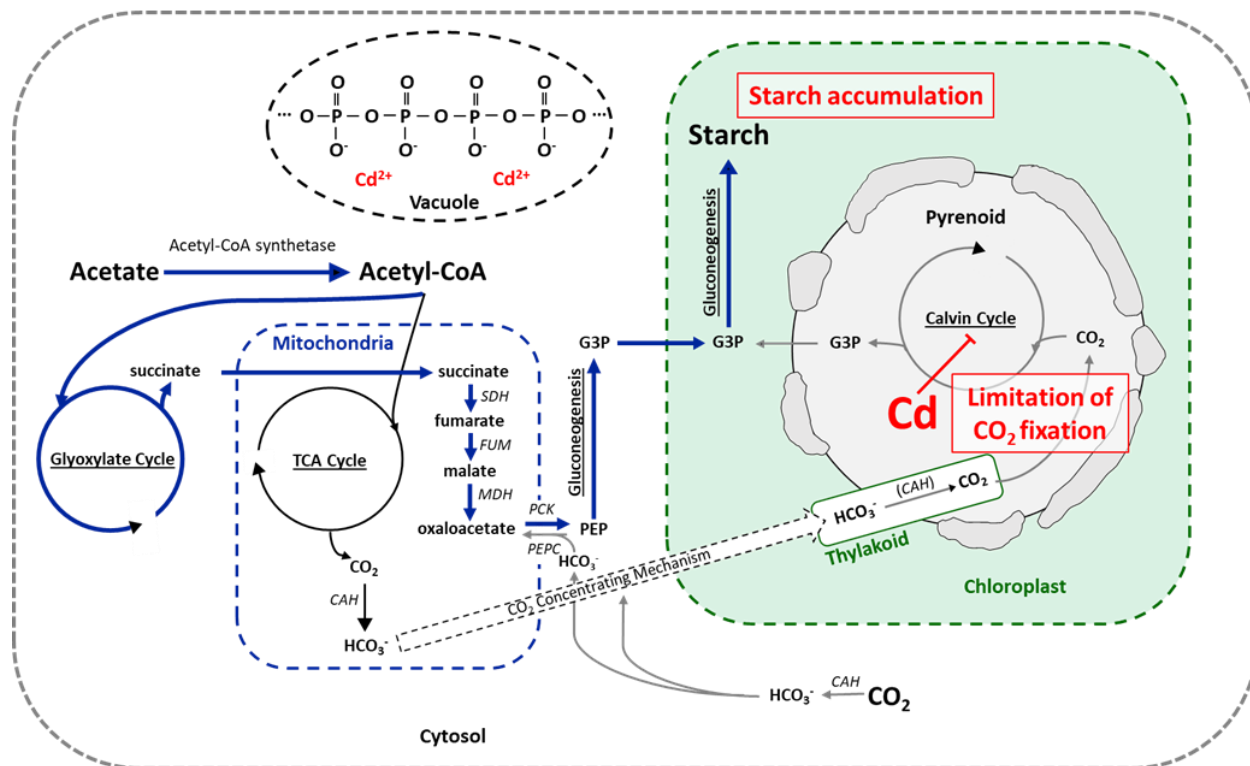
1107

1108

1109

1110

Figure 5



1111